

Nitrogen partitioning between branched-chain amino acids and urea cycle enzymes sustains renal cancer progression

Marco Sciacovelli^{*1}, Aurelien Dugourd^{2,3,4*}, Lorea Valcarcel Jimenez¹, Ming Yang¹, Efterpi Nikitopoulou¹, Ana S.H.Costa^{1,5}, Laura Tronci¹, Veronica Caraffini¹, Paulo Rodrigues¹, Christina Schmidt¹, Dylan Ryan¹, Tim Young¹, Vincent R. Zecchini¹, Sabrina Helena Rossi⁶, Charlie Massie⁶, Caroline Lohoff², Maria Masid Barcon⁷, Vassily Hatzimanikatis⁷, Christoph Kuppe^{8,9,10}, Alex Von Kriegsheim¹¹, Rafael Kramann^{8,9,10}, Vincent Gnanapragasam¹³, Anne Y. Warren¹⁴, Grant D. Stewart¹³, Ayelet Erez¹⁵, Sakari Vanharanta¹, Julio Saez-Rodriguez^{2,3*} and Christian Frezza^{1*}.

¹ Medical Research Council Cancer Unit, University of Cambridge- Hutchison/MRC Centre, Box 197 Biomedical Campus-CB20XZ Cambridge UK.

² Institute for Computational Biomedicine, Faculty of Medicine, Heidelberg University and Heidelberg University Hospital, BioQuant, Heidelberg, Germany

³ Joint Research Center for Computational Biomedicine, RWTH Aachen University Hospital, Aachen, Germany

⁴ Institute of Experimental Medicine and Systems Biology, RWTH Aachen University, Aachen, Germany

⁵ Cold Spring Harbor Laboratory, Cold Spring Harbor, NY 11724, USA.

⁶ Early Detection Programme, CRUK Cambridge Centre, Department of Oncology, University of Cambridge, Hutchison/MRC Centre, Box 197 Biomedical Campus-CB2 0XZ-Cambridge UK

⁷ Ecole polytechnique fédérale de Lausanne, Institut des sciences et ingénierie chimiques EPFL, CH H4 625 (Bât. CH) Station 6- CH-1015 Lausanne, Switzerland.

⁸ Division of Nephrology and Clinical Immunology, Faculty of Medicine, RWTH Aachen University, Aachen, Germany.

⁹ Department of Internal Medicine, Nephrology and Transplantation, Erasmus Medical Center, Rotterdam, The Netherlands.

¹⁰ Institute of Experimental Medicine and Systems Biology, RWTH Aachen University, Aachen, Germany

¹¹ Edinburgh Cancer Research UK Centre, Institute of Genetics and Molecular Medicine, Crewe Road South-EH4 2XR Edinburgh UK

¹³ Department of Surgery, University of Cambridge and Cambridge University Hospitals NHS Cambridge Biomedical Campus, Cambridge, UK.

¹⁴ Dept of Histopathology-Cambridge University Hospitals NHS, Box 235 Cambridge Biomedical Campus - CB2 0QQ

¹⁵ Department of Biological Regulation, Weizmann Institute of Science, Rehovot, Israel

*= equal contribution

Correspondence should be addressed to:

C.F. (CF366@cam.ac.uk)

J.S.R. (julio.saez@bioquant.uni-heidelberg.de)

SUMMARY

Metabolic reprogramming is critical for tumor initiation and progression. However, the exact impact of specific metabolic changes on cancer progression is poorly understood. Here, we combined multi-omics datasets of primary and metastatic clonally related clear cell renal cancer cells (ccRCC) and generated a computational tool to explore the metabolic landscape during cancer progression. We show that a *VHL* loss-dependent reprogramming of branched-chain amino acid catabolism is required to maintain the aspartate pool in cancer cells across all tumor stages. We also provide evidence that metastatic renal cancer cells reactivate argininosuccinate synthase (*ASS1*), a urea cycle enzyme suppressed in primary ccRCC, to enable invasion *in vitro* and metastasis *in vivo*. Overall, our study provides the first comprehensive elucidation of the molecular mechanisms responsible for metabolic flexibility in ccRCC, paving the way to the development of therapeutic strategies based on the specific metabolism that characterizes each tumor stage.

Key words

branched-chain amino acids, BCAT1, *ASS1*, metastasis, clear cell renal cell carcinoma (ccRCC), aspartate, *VHL*, arginine, urea cycle, metabolomics visualization

Highlights

1. Branched-chain amino acids catabolism is reprogrammed in ccRCC tumors

- 57 2. BCAT-dependent transamination supplies nitrogen for *de novo* biosynthesis of amino
58 acids including aspartate and asparagine in ccRCC
- 59 3. Aspartate produced downstream of BCAT is used specifically by metastatic cells
60 through argininosuccinate synthase (ASS1) and argininosuccinate lyase (ASL) to
61 generate arginine, providing a survival advantage in the presence of microenvironments
62 with rate limiting levels of arginine
- 63 4. ASS1 is re-expressed in metastatic 786-M1A through epigenetic remodeling and it is
64 sensitive to arginine levels
- 65 5. Silencing of ASS1 impairs the metastatic potential *in vitro* and *in vivo* of ccRCC cells

66

67 INTRODUCTION

68 Cancer is an ever-evolving disease in which tumor cells are subject to constant changes in
69 nutrient and oxygen availability within the tumor microenvironment. To adapt to different
70 microenvironments during tumor evolution, cancer cells become metabolically flexible, a
71 process orchestrated either directly by metabolites availability or by activation of oncogenic
72 signaling (Fendt et al., 2020). Consistently, it has been shown that tumors at different stages
73 are metabolically distinct (Bergers and Fendt, 2021; Elia et al., 2018; Kreuzaler et al., 2020;
74 Pascual et al., 2018; Pavlova and Thompson, 2016; Vander Heiden and DeBerardinis, 2017).
75 For instance, solid tumors use nutrients such as glucose to generate the biomass necessary to
76 sustain their high proliferative demands (Pavlova and Thompson, 2016; Vander Heiden and
77 DeBerardinis, 2017), whereas successful metastasis relies more on pyruvate, glutamine, lipid
78 metabolism and, in specific tumor types, on mitochondrial metabolism such as oxidative
79 phosphorylation (Bergers and Fendt, 2021; Vander Heiden and DeBerardinis, 2017)

80 High-throughput metabolomics technologies are widely used to study cancer metabolism.
81 However, despite the simultaneous measurement of hundreds of metabolites, this approach
82 cannot fully capture the complexity and dynamics of the altered metabolic network. Therefore,
83 it is crucial to develop computational algorithms that can extract more biological insight from
84 sparse metabolomics data (Aurich and Thiele, 2016; Berg et al., 2020; Dugourd et al., 2021).
85 These methods, combined with *in vitro* experimental conditions that mimic the nutrient
86 microenvironment of the tumor *in vivo* (Cantor et al., 2017; Vande Voorde et al., 2019), can be
87 used not only to dissect the complexity of tumor metabolism regulation, but also to identify
88 new metabolic vulnerabilities *in vivo*.

89 Clear cell renal cell carcinoma (ccRCC), the most common histological subtype of RCC that
90 accounts for 70% of renal malignancies (Choueiri and Motzer, 2017), has been extensively
91 studied for its profound metabolic reprogramming (Gatto et al., 2014; Hakimi et al., 2016;
92 Wettersten et al., 2017). ccRCC arises from epithelial tubular cells (Young et al., 2018) and is
93 driven by (epi)genetic lesions affecting the tumor suppressor Von Hippel-Lindau (*VHL*) gene.
94 *VHL* loss leads to robust activation of pro-oncogenic signaling mediated by the Hypoxia
95 Inducible Factor 2A (*EPAS1/HIF2A*) (Clark et al., 2019; Creighton et al., 2013; Ricketts et al.,
96 2018), which transcriptionally orchestrates some of the most prominent metabolic alterations
97 of these tumors. ccRCC tumors are fueled by aerobic glycolysis rather than oxidative
98 phosphorylation (OXPHOS) due to HIF-mediated metabolic reprogramming and the
99 mitochondrial dysfunction frequently observed in these tumors (LaGory et al., 2015; Nam et
100 al., 2021; Wettersten et al., 2017). Over the last years, other pathways were added to the
101 metabolic landscape of ccRCC, including dysregulated tryptophan, arginine and glutamine
102 metabolism, together with enhanced lipid and GSH biosynthesis (Wettersten et al., 2017). Only
103 recently, it was shown that the genomic loss or suppression of urea cycle (UC) genes such as

104 Arginase 2 (*ARG2*) and argininosuccinate synthetase (*ASS1*) favors renal cancer growth,
105 preserving the consumption of pyridoxal 5'-phosphate (Ochocki et al., 2018). ccRCC tumors
106 are also metabolically flexible, and the metabolic landscape of late-stage renal cancers is
107 distinct from that of primary renal tumors. More specifically, it was shown that upregulation
108 of GSH biosynthesis, cysteine/methionine metabolism and polyamine pathways is associated
109 with advanced ccRCC (Hakimi et al., 2016). However, how the metabolic landscape of renal
110 tumors evolves through progression, is regulated at molecular level and impacts on tumor
111 biology is largely unknown.

112 In this study, we performed a systemic analysis of ccRCC tumors and a multi-omic study of a
113 panel of primary and metastatic cancer cells cultured in physiological media to identify altered
114 metabolic pathways in renal cancer progression. We show that the reprogramming of branched-
115 chain amino acids (BCAAs) is a distinctive metabolic alteration of ccRCC to support aspartate
116 generation, independently from the tumor stage. We also demonstrate that whilst some UC
117 enzymes are deficient in primary renal cancer cells, one of the UC enzymes, *ASS1*, is
118 epigenetically reactivated in the metastatic populations. We further demonstrated that *ASS1*
119 expression is required to maintain the invasive potential of metastatic renal cancer cells *in vitro*
120 and *in vivo*. Finally, we show that *ASS1* expression leads to reduced sensitivity of metastatic
121 cancer cells to arginine depletion and enables metastasis homing in the lungs. Our data indicate
122 the presence and dynamics of stage-specific metabolic adaptations, which could be used to
123 identify novel therapeutic targets and optimize current clinical protocols, especially for late-
124 stage disease.

125

126 RESULTS

127 BCAA catabolism is transcriptionally suppressed in primary and metastatic ccRCC

128 To identify metabolic pathways reprogrammed in ccRCC progression, we first performed an
129 enrichment analysis (GSEA) of tumor *vs* matched normal tissue using the renal clear cell
130 carcinoma (KIRC) RNA-seq dataset from The Cancer Genome Atlas (TCGA) (Figure 1A). We
131 identified amongst the most upregulated pathways in the tumors ribosome, DNA replication
132 and signaling cascades while key metabolic features dysregulated in ccRCC tumors included
133 not only the suppression of OXPHOS and TCA cycle but also arginine, BCAAs, tryptophan,
134 and pyruvate metabolism (Figure 1A), in line with previous findings (Clark et al., 2019; Gaude
135 and Frezza, 2016; Hakimi et al., 2016; Li et al., 2014; Pandey et al., 2020). Of note, BCAA
136 catabolism (valine, leucine and isoleucine degradation) was the most suppressed pathway in
137 renal tumors. Interestingly, all the genes of the pathway were significantly downregulated in
138 the tumor samples, with the exception of the Branched Chain Amino Acid Transaminase 1
139 (*BCAT1*) and the lysosomal amino acids oxidase Interleukin 4 Induced 1 (*IL4I1*), which were
140 strongly upregulated (Figure 1B). This apparent discrepancy between the expression of *BCAT1*
141 and the other genes from the BCAA catabolism suggests that additional mechanisms beyond
142 the transcriptional control may be involved in the fine tuning of the pathways in tumors.

143 Then, we focused on metabolic pathways that are transcriptionally deregulated during ccRCC
144 progression. To this end, we compared RNA-seq from patients locally advanced and metastatic
145 (stage III+IV) *vs* localized (stage I+II) ccRCC tumors. Using this approach, we identified
146 metabolic pathways suppressed in stage III-IV cancers, with the BCAA catabolism as the top
147 downregulated one (Figure 1C). Consistent with a role for BCAA catabolism in ccRCC
148 progression, the overall survival of patients with ccRCC correlated with the expression level
149 of this pathway (Figure 1D), with high expression associated with better prognosis. Of note, a

150 significant correlation between BCAA enzyme levels and patient survival was only observed
151 in a few tumor types, including renal cancer (KIRC and kidney renal papillary cell carcinoma
152 KIRP) and colorectal cancer (Figures S1A-B). Thus, the suppression of BCAA catabolism is a
153 metabolic hallmark of renal cancer and is independent from the cancer stage.

154 **BCAA catabolism is reprogrammed in ccRCC cancer cells cultured in physiological** 155 **medium**

156 To assess the role of BCAA catabolism in renal cancer, we compared HK-2 proximal tubule
157 kidney epithelial cells with a panel of ccRCC cell lines, 786-O, OS-RC-2, RFX-631 and the
158 metastatic derivatives, 786-M1A, 786-M2A, and OS-LM1 (Vanharanta et al., 2013) (Figure
159 2A). To mimic the nutrient availability *in vivo*, we cultured all the cell lines in Plasmax, a
160 recently developed physiological medium based on the human serum's nutrient composition
161 (Vande Voorde et al., 2019). First, we performed a liquid chromatography-mass spectrometry
162 (LC-MS) metabolomic analysis of the cells stably grown in Plasmax or in standard culture
163 medium (RPMI) and correlated it with the metabolic profile of a cohort of renal tumors and
164 matched healthy renal tissues (Dugourd et al., 2021). The metabolic profiles of cells grown in
165 Plasmax exhibited a significant correlation with the profiles of tumor and normal tissues (p -
166 value $< 10^{-6}$) which is slightly higher compared to that of cells cultured in RPMI (p -value $< 10^{-8}$)
167 (Figure S2A). Furthermore, when we analyzed their transcriptomic profile, ccRCC cells
168 grown in Plasmax displayed the activation of transcription factors (TF) such as the Hypoxia-
169 inducible Factor 1B (HIF1B, *ARNT* gene), Hypoxia-inducible Factor 2A (HIF2A, *EPAS1*
170 gene), MYC Associated Factor X (*MAX*), and Paired Box 8 (*PAX8*), known drivers of ccRCC
171 (Bleu et al., 2019; Creighton et al., 2013; Vanharanta et al., 2013). Consistent with previous
172 data (Rodrigues et al., 2018; Vanharanta et al., 2013), the metastatic cell lines maintained the
173 expression of specific metastatic markers such as the C-X-C Motif Chemokine Receptor 4
174 (*CXCR4*), the Cytohesin 1 Interacting Protein (*CYTIP*), the Latent Transforming Growth Factor
175 Beta Binding Protein 1 (*LTBP1*) and the SLAM Family Member 8 (*SLAMF8*) (Figure S2C).

176 We then investigated the differential expression of the metabolic pathways in the renal cells
177 HK2, 786-O and 786-M1A using proteomics. Enrichment analysis of proteomics data indicated
178 that glycolysis, purine and glutathione metabolism were upregulated while the BCAA
179 catabolism, together with the OXPHOS and the TCA cycle, were amongst the most suppressed
180 metabolic pathways in both 786-O and 786-M1A when compared with HK2 cells (Figure 2B),
181 in line with the results of the renal tumors from patients (Figures 1A). Importantly, the majority
182 of the proteins detected that belong to the BCAA catabolism were suppressed in 786-O vs HK2
183 cells with the exception of a few enzymes including BCAT1, Short/Branched Chain Specific
184 Acyl-CoA Dehydrogenase (ACADSB) and the Aldehyde Dehydrogenase 2 (ALDH2). (Figure
185 S2D). Notably, the levels of both BCAA catabolism and OXPHOS related proteins were further
186 suppressed in metastatic 786-M1A compared to primary 786-O (Figure 2C), as observed in the
187 most aggressive renal tumors (Figure 1C). The suppression of the OXPHOS in all renal cancer
188 cells was confirmed by the lower basal and stimulated cellular respiration compared to HK2
189 cells (Figure S2E). To functionally validate the GSEA results, we used our metabolomics data
190 (Figure 2D-E). We observed that both 786-O and 786-M1A have lower intracellular levels of
191 leucine and isoleucine, while they accumulated C5 carnitines and methylmalonyl-carnitine, by-
192 product metabolites derived from intermediates of BCAA catabolism, while no significant
193 differences were observed in C3-carnitines (Figures 2D-F; S2F). The accumulation of by-
194 product metabolites derived from intermediates of BCAA catabolism might be the consequence
195 of the suppression of key acyl-CoA dehydrogenases that belong to the BCAA catabolism such
196 as Isovaleryl-CoA dehydrogenase (IVD) and Methylmalonyl-CoA mutase (MUT) (Figure 2G).

197 Intriguingly, 786-M1A metastatic cells displayed a higher accumulation of methylmalonyl-
198 carnitine when compared to 786-O cells (Figure 2E-S2F) suggesting a potential enhanced
199 deregulation of BCAA catabolism. Finally, the uptake of the BCAAs was substantially
200 unaltered across all cell lines, (Figure S2G). even though the heterodimer transport system
201 between the Solute Carrier Family 7 Member 5 (SLC7A5, LAT1) and Solute Carrier Family 3
202 Member 2 (SLC3A2, CD98) (Figures S2H) was upregulated in all ccRCC cells compared to
203 HK2 cells.

204 In summary, these data show that this ccRCC cellular model cultured using a physiological
205 formulation called Plasmax recapitulates the transcriptomic, proteomic, and metabolic features
206 of ccRCC patients at different stages of progression, including the suppression of BCAA
207 metabolism.

208 **Metabolic deregulation of BCAA catabolism in ccRCC**

209 To further characterize the metabolic landscape of ccRCC cells during progression, including
210 the reprogramming of BCAA catabolism, we applied ocEAn (metabOliC Enrichment
211 Analysis) to our metabolomics data, a computational method that generates a metabolic
212 footprint for each metabolic enzyme present in the recon 2 metabolic reaction network (Figure
213 S3A, methods). These footprints show the metabolites directly or indirectly associated with a
214 given metabolic enzyme, their abundances and relative position either upstream or downstream
215 of the reaction. Through the metabolic footprints, ocEAn provides an overview of the metabolic
216 alterations centered on the single enzyme, highlighting patterns of imbalance between the
217 upstream and downstream metabolites mapped in the enzyme footprint (Figure S3A, full
218 interactive network available at: <https://sciacovelli2021.omnipathdb.org>). We applied this tool
219 to study the activity of BCAT1, a key enzyme at the entry point of BCAA catabolism in our
220 renal cellular models. BCAT1 was found upregulated both in the tumors from TCGA (Figure
221 1B) and in ccRCC cells at the protein level (Figure S2D). All ccRCC cells displayed lower
222 BCAAs levels upstream of BCAT1 with a significant up-regulation of carnitines derived from
223 intermediates of the BCAA catabolism, notably methyl-malonyl-carnitine ($\log_2 \text{FC} > 2$, FDR
224 $< 10^{-40}$) and C5-carnitines downstream of the reaction (Figure 3A, Figure S2F). One of the
225 benefits of ocEAn is the possibility to uncover deregulated metabolites indirectly associated
226 with an enzyme, either upstream or downstream, that might contribute to its biological
227 function. Intriguingly, we found that argininosuccinate, an intermediate product of the urea
228 cycle strongly down-regulated in 786-O compared to HK2, was the top upregulated metabolite
229 downstream of BCAT1 in the metastatic 786-M1A cells when compared to 786-O (Figure 3A).
230 This result suggests that some products of BCAT transamination are shunted in the urea cycle
231 in the renal cancer cells and also that the functioning of the urea cycle might differ between
232 786-M1A vs 786-O. In summary, we developed a new computational tool to visualize
233 metabolomics datasets that can capture the network of the metabolic reprogramming of cancer
234 cells.

235 **BCAA catabolism does not generate carbons for the TCA cycle in ccRCC cells**

236 To understand the biological relevance of the BCAA catabolism reprogramming in ccRCC
237 progression and its involvement in the acyl-carnitines accumulation, we cultured HK2, 786-O
238 and the derived metastatic cells (786-M1A and 786-M2A) together with additional ccRCC cells
239 (OS-RC-2 and metastatic derivatives OS-LM1; RFX-631, Figure 2A) in the presence of $^{13}\text{C}_6$
240 leucine+isoleucine and we measured the generation of labelled downstream metabolites,
241 including KIC/KMV, C5 and C3-carnitines and TCA cycle intermediates fumarate and malate
242 (Figure S3B). We detected higher labelling in both C5 carnitines and C3 carnitines (C5-

243 carnitine m+5 and C3 carnitine m+3) in all cancer cells at 1h and 3h time points compared to
244 HK2 (Figure 3B) while leucine+isoleucine or KIC+KMV labelled percentages were similar
245 among all cells. These results showed that the upper part of the BCAA catabolism is still
246 functional in all renal cancer cells, even more active in ccRCC than normal HK2, independently
247 from the tumor stage. However, the full oxidation of BCAAs did not significantly contribute
248 to the generation of TCA cycle intermediates in all renal cells since we detected a very low
249 fraction of labelled fumarate (3%) and malate (below 1%) (Figure 3B). We incubated HK2,
250 786-O and the derived metastatic cells with the ¹³C₆ leucine+isoleucine for a longer time (43h),
251 but similarly to the shorter time points, the labelled percentages of both C2-carnitines and
252 fumarate were below 1% despite comparable levels of labelled intracellular leucine (Figure
253 S3C). Whilst the very low percentage of labelled C2-carnitine might be due to the presence of
254 C2-carnitine in the medium, these results are consistent with previous reports that showed a
255 limited contribution of BCAAs oxidation in the TCA cycle *in vivo* in the kidneys (Neinast et
256 al., 2019b) and other tumor types (Raffel et al., 2017; Sivanand and Vander Heiden, 2020). In
257 conclusion, these tracing experiments confirmed that BCAA degradation is deregulated in
258 ccRCC and BCAAs are not used as substrates in the TCA cycle.

259 **BCAT transamination provides nitrogen for the biosynthesis of aspartate in renal cancer** 260 **cells and arginine in metastatic derivatives**

261 The BCAA catabolism represents an important source of nitrogen for amino acids synthesis,
262 based on the production of glutamate through transamination of BCAA by BCATs (Neinast et
263 al., 2019a; Sivanand and Vander Heiden, 2020). We have shown that the BCAAs are not
264 significantly contributing to generation of the TCA cycle intermediates in all the renal cells
265 used (Figure 3B and Figure S3C) and moreover, ocEAn highlighted the significant
266 deregulations of aspartate, asparagine and argininosuccinate downstream of BCAT1 (Figure
267 3A). Therefore, we hypothesized that the reprogramming we observed in ccRCC might provide
268 a nitrogen source for the generation of glutamate and other downstream metabolic reactions.
269 To experimentally validate the biological role of BCAT transamination we cultured HK2, 786-
270 O and 786-derived metastatic cells in the presence of ¹⁵N leucine+isoleucine in Plasmax and
271 measured the generation of ¹⁵N-labelled glutamate (Figure 4A). Glutamate is a key amino acid
272 used in multiple metabolic pathways. For instance, it donates the nitrogen for the conversion
273 of oxaloacetate into aspartate catalyzed by Glutamate Oxaloacetate Transaminases
274 (GOT1/GOT2), which through asparagine synthase (ASNS) can be in the end converted into
275 asparagine (Figure 4A). We found that all ccRCC cells generated significantly more glutamate,
276 aspartate, and asparagine labelled from leucine and isoleucine (Figures 4B-C; Figure S4A).
277 Among other glutamate-derived amino acids, we also detected increased labelling in proline
278 (proline m+1) in 786-O, 786-M1A and 786-M2A, while serine, glutamine and alanine m+1
279 were lower than HK2 cells (Figure S4A). To derive aspartate from leucine, cancer cells rely on
280 the reverse reaction of GOTs, which consumes glutamate derived from leucine transamination
281 and OAA to generate α KG and aspartate (Mayers et al., 2016). In line with this observation,
282 GOT1 protein levels were higher in ccRCC cells, while on the contrary, GOT2 was suppressed
283 (Figure S4B). Similarly, we also detected an increase in ASNS protein levels in all renal cancer
284 cells, in line with the increased labelling of asparagine in ccRCC (Figure S4B). Of note, a
285 similar metabolic rewiring was observed in OS-RC-2, OS-LM1 and RFX-631, that derived a
286 higher amount of glutamate, aspartate, and asparagine from BCAA when compared to normal
287 HK2 cells (Figures S4C). To better understand the maximal contribution of BCAT
288 transamination to the generation of aspartate, we cultured the cells in EBSS where exogenous
289 aspartate, glutamate and other amino acids are absent, with the exception of ¹⁵N leucine.
290 Strikingly, the net contribution of BCAT transamination to *de novo* generation of aspartate in
291 these conditions reaches more than 60% in renal cancer cells (Figure 4D), while in HK2 cells

292 it is below 20% even though the intracellular percentage of labelled leucine in all cell types is
293 comparable (Figure S4D). We did not observe differences in the relative percentage of the
294 labelled glutamate in these conditions among the cells, even though the abundance of glutamate
295 m+1 is still higher in ccRCC cells (Figure 4D). Considering that aspartate is limiting for
296 nucleotide biosynthesis (Alkan and Bogner-Strauss, 2019; Garcia-Bermudez et al., 2018), we
297 then assessed whether BCAT1 activity indirectly contributes to nucleotide pools. To test this
298 hypothesis, we suppressed BCAT activity with a pharmacological inhibitor (BCAT inhibitor
299 2, BCATI, Figure 4A), which preferentially targets the cytosolic BCAT1 isoform (McBrayer
300 et al., 2018). As a result of the BCAT inhibition, we observed a suppression of both the BCKAs
301 downstream of BCAT in all cell types, together with C5-carnitines (Figure S4C). Importantly,
302 the inhibition of the transamination also affected glutamate and the intracellular aspartate levels
303 even though the last one mainly in metastatic cells (Figure 4E). As a consequence of the
304 alterations of the aspartate pool induced by BCATI, the levels of carbamoyl-aspartate,
305 dihydroorotate, and uridine monophosphate (UMP), all intermediates of *de novo* pyrimidine
306 biosynthesis, together inosine monophosphate (IMP) from purine biosynthesis pathways, were
307 significantly decreased in 786-O cancer cells and their metastatic derivatives (Figure 4F-G). In
308 summary, we found that the reprogramming of BCAA degradation supports the generation of
309 aspartate and nucleotide biosynthesis through BCAT transamination in both primary and
310 metastatic ccRCC cells.

311 **VHL loss reprograms BCAA catabolism in ccRCC cells**

312 We then investigated the molecular mechanisms underpinning the dysregulation of BCAA
313 metabolism in ccRCC. *VHL* loss is a key driver in ccRCC formation, and through HIF
314 activation, it is responsible for the metabolic and bioenergetic reprogramming of renal cancer
315 (Wettersten et al., 2017). There is also evidence that under hypoxia, both HIF1A and HIF2A
316 can transcriptionally regulate some of the genes of the BCAA catabolism such as *BCAT1* and
317 *SLC7A5* in different tumor types (Elorza et al., 2012; Onishi et al., 2019; Zhang et al., 2021).
318 Therefore, we investigated whether the rewiring of the BCAA catabolism in ccRCC depends
319 on *VHL* loss. To address this question, we re-expressed wild-type *VHL* in 786-O and 786-M1A
320 cells (Figure S5A). *VHL* expression restored mitochondrial respiration (Figure S5B) and
321 increased aspartate level (Figure S5C). Next, we performed an enrichment analysis to identify
322 which pathways are differentially regulated by *VHL* using additional proteomics data.
323 Surprisingly, we found that BCAA catabolism is one of the most upregulated pathways in both
324 786-O and 786-M1A cells upon *VHL* restoration (Figures 5A-B). As a consequence of the
325 *VHL*-mediated transcriptional reprogramming, 786-O+*VHL* and 786M1A +*VHL* cells showed
326 significant suppression of C5 and C3 carnitines accumulation (Figure 5C). To assess the
327 functionality of the BCAA catabolism, we cultured HK2, 786-O and 786-M1A±*VHL* with $^{13}\text{C}_6$
328 leucine and we measured the generation of labelled metabolites downstream of leucine
329 including KIC and C5-carnitines. In these conditions, we did not observe relevant changes in
330 the relative percentage of labelling of both KIC and C5-carnitines derived from ^{13}C leucine,
331 whose levels are similar in all cell types (Figure S5D). However, we observed that *VHL*
332 restoration induced almost 50% suppression of *SLC7A5*, the BCAA main transporter (Figure
333 5E). Together with the re-expression of key proteins that belong to BCAA catabolism (Figure
334 5B), the reduction of *SLC7A5* mRNA upon *VHL* re-expression confirmed that *VHL* loss is
335 involved, at least in part, in the reprogramming of the BCAA degradation in renal cancer cells.

336 **Argininosuccinate synthase (ASS1) is epigenetically reactivated in metastatic ccRCC and** 337 **confers cells with resistance to arginine depletion**

338 We then focused on the metabolic changes specific to the transition toward metastasis in the
339 786-O cellular model. Interestingly, ocEAn identified argininosuccinate, a urea cycle
340 intermediate produced by argininosuccinate synthase (ASS1), as one of the key upregulated
341 metabolites in metastatic cells compared to 786-O downstream of BCAT1 (Figure 3A).
342 Importantly, the nitrogen tracing experiments revealed the unexpected finding that the nitrogen
343 from BCAAs was channeled into the biosynthesis of arginine through labelled aspartate, which
344 is required to generate argininosuccinate by ASS1, in the metastatic 786-M1A and 786-M2A
345 cells but not in normal HK2 or 786-O cells (Figure 6A, Figure S4A). Of note, the abundance
346 of labelled argininosuccinate is higher in the metastatic cells compared to HK2 (Figure 6A).
347 Since *ASS1* is known to be suppressed in 786-O and ccRCC (Ochocki et al., 2018), we
348 speculated that *ASS1* might be reactivated in metastatic 786-M1A and 786-M2A cells.
349 Accordingly, we detected higher ASS1 protein levels in metastatic cells compared to 786-O,
350 with a mild increase in ASS1 levels even though not statistically significant while ARG2 was
351 strongly suppressed as shown before (Ochocki et al., 2018) (Figure S6A). To evaluate the
352 specificity of ASS1 re-expression in the metastatic cells, we first focused on the metabolic
353 genes differentially expressed between primary 786-O and metastatic 786-M1A cells cultured
354 in Plasmax, using RNA-seq data (Figure 6B). This analysis revealed that *ASS1* was among the
355 top upregulated metabolic genes in the metastatic cells together with Aldo-Keto Reductase
356 Family 1 Member (*AKR1B1*), Aldehyde Dehydrogenase 2 (*ALDH2*) and Glucose-6-phosphate
357 dehydrogenase (*G6PD*). We confirmed that ASS1 protein levels are restored in 786-derived
358 metastatic cells using western blot (Figure S6B) and that ASS1 expression was associated with
359 increased intracellular levels of argininosuccinate in 786-M1A and 786-M2A (Figure 6C)
360 compared to 786-O. Despite a differential regulation of *ASS1* among all the renal cell lines, we
361 did not detect differences in the arginine uptake, except for 786-M2A cells, where it was
362 considerably reduced compared to HK2. We also observed a higher release of ornithine in HK2
363 cells, while citrulline was selectively taken up only by the metastatic cells, which might be
364 linked to ASS1 re-expression and its requirement for argininosuccinate biosynthesis (Figure
365 S6C).

366 Next, we investigated how ASS1 expression was controlled in these cell lines. Based on
367 previous reports showing hypermethylation of the *ASS1* promoter region and consequent gene
368 suppression in different tumor types (Allen et al., 2014; Huang et al., 2013; Lan et al., 2014;
369 McAlpine et al., 2014; Nicholson et al., 2009; Syed et al., 2013), we hypothesized that changes
370 in methylation of *ASS1* promoter might control *ASS1* expression. Thus, we focused on a CpG
371 island (hg38-chr9:130444478-130445423) that overlaps with the transcription starting site
372 (TSS) of the gene (GRch38 chr9:130444200-130447801) and we measured its methylation
373 using TruSeq Methyl Capture EPIC. We observed a gain of methylation at several CGs within
374 this CpG island in 786-O, where *ASS1* is suppressed, while the same region is relatively
375 hypomethylated in metastatic 786-M1A similarly to HK2 cells (Figure 6D), where the gene is
376 highly expressed. Importantly, treatment of 786-O with 5-azacitidine (5AC), a DNA
377 methylation inhibitor, significantly increased *ASS1* expression, supporting the hypothesis that
378 *ASS1* is epigenetically suppressed in primary renal cancer cells (Figure 6E). Furthermore, we
379 detected a strong peak of H3K27ac present at *ASS1* TSS in 786-M1A cells, which reflects the
380 increased transcription of the gene (Figure S6D).

381 Next, we assessed if the reactivation of *ASS1* is a common phenomenon associated with the
382 selection of metastatic cells by determining *ASS1* expression in the metastatic counterparts of
383 OS-RC-2, the OS-LM1 cells which we generated previously (Figure 2A). However, in this
384 different metastatic model *ASS1* mRNA is marginally upregulated in metastatic OS-LM1
385 compared to OS-RC-2 (Figure S6E) even though ASS1 was strongly suppressed in both ccRCC

386 cells when compared to HK2 cells at the protein level (Figure S6F). Similarly to 786-O, the
387 CpG island overlapping with the *ASS1* TSS is strongly hypermethylated in OS-RC-2, although
388 we did not observe any change in its methylation levels in OS-LM1 (Figure S6G). We
389 confirmed that in these cells *ASS1* is epigenetically controlled by methylation since the
390 treatment with 5AC leads to the re-expression of the gene in both cell lines (Figure S6H).
391 Together, these data suggested that *ASS1* is epigenetically controlled in some but not all
392 metastatic renal cancer cells. Therefore, *ASS1* upregulation might not be present in all advanced
393 ccRCC tumors. To further corroborate this hypothesis, we analyzed changes in *ASS1*
394 expression in human tumors from the TCGA RNA-seq dataset. Based on *ASS1* expression, we
395 identified a cluster of advanced ccRCC (*ASS1*^{high} around 10% of the total cohort of cancers
396 from stage III+IV) in which *ASS1* is significantly upregulated compared to stage I+II tumors,
397 consistently with the phenotype observed in 786-M1A cells (Figure S6I). Intriguingly, this
398 group of tumors is characterized by distinctive metabolic phenotype (Figure S6J) including
399 upregulation of glycine, serine and threonine metabolism, aspartate and glutamate metabolism,
400 and OXPHOS which strongly diverged from *ASS1*^{low} stage III+IV tumors (Figure S6J). Finally,
401 we measured the accumulation of argininosuccinate in a small cohort (N=18) of primary
402 ccRCC from patients we recently collected that were metastatic at time of diagnosis. As shown
403 in Figure S6K, some of the metastatic tumors showed an increase in argininosuccinate levels
404 compared to matched healthy tissue suggesting that *ASS1* expression in advanced ccRCC might
405 be heterogeneous.

406 It has been proposed that the suppression of *ASS1* induces arginine auxotrophy, sensitizing
407 cancer cells to arginine depletion. Our results suggest that primary and metastatic cells may
408 exhibit a different sensitivity to arginine depletion. Consistently, we found that the metastatic
409 786-M1A and 786-M2A were resistant to arginine depletion using the pegylated arginine
410 deiminase (ADIPEG20), as a consequence of the restoration of *ASS1* in these cells (Figure 6F).
411 Given that *ASS1* expression confers the cells with the ability to survive in absence of arginine,
412 we hypothesized that the depletion of arginine might regulate *ASS1* expression in the renal
413 cancer cells. Therefore, we chronically treated 786-O cells, where *ASS1* is silenced, with
414 ADIPEG20. Initially, the cells stopped proliferating until some subclones, resistant to the
415 treatment, started to emerge. *ASS1* expression was upregulated in this population at mRNA
416 level, corroborating the hypothesis of a pro-survival role of *ASS1* when arginine is rate-limiting,
417 accompanied by a significant increase in the expression of the metastasis mediator *CXCR4*
418 (Figure 6G).

419 Based on these results we hypothesized that during tumor progression, renal cancer cells might
420 be exposed to microenvironments that differ in arginine content. To corroborate this
421 hypothesis, we measured the arginine levels in different mouse organs and their tissue
422 interstitial fluids, focusing on the comparison between the kidneys and the lungs, the organ
423 colonized by the metastatic population. Strikingly, arginine levels were significantly reduced
424 in both the tissue and the interstitial fluid in the lungs compared to the kidneys (Figure S6L),
425 suggesting that differences in arginine availability might directly contribute to the selection
426 of metastatic subpopulations that re-express *ASS1* in the lungs.

427 Collectively, we identified *ASS1* as one of the most differentially regulated metabolic genes in
428 metastatic ccRCC. We demonstrated that *ASS1* re-expression enables metastatic cells to
429 survive under arginine limiting conditions. Intriguingly, *ASS1* expression is epigenetically
430 controlled in 786-O cells and can be triggered by arginine depletion. Differential arginine
431 availability between the organs might contribute to the selection of aggressive *ASS1*-proficient
432 renal cancer cells and to metastatic homing in the lungs.

433 **ASS1 silencing impairs the metastatic potential of renal cancer cells**

434 Finally, we assessed whether ASS1 re-expression contributes to the metastatic features of this
435 cell line. We observed that in 786-O cells treated chronically with ADIPEG, ASS1 increased
436 expression was associated with CXCR4 increase (Figure 6G). On the other hand, silencing of
437 ASS1 (Figure 6H) did not affect proliferation of 786-M1A but it strongly impaired the invasive
438 growth of spheroids in collagen I matrixes, indicating that ASS1 is required for the invasion
439 and migration of metastatic cells *in vitro* (Figure 6J). Based on the resistance to arginine
440 depletion and the effects of ASS1 silencing *in vitro*, we tested its effect on metastatic
441 colonization and survival *in vivo*. Indeed, when injected into the tail vein of
442 immunocompromised mice, 786-M1A+shASS1#1 and 786-M1A+shASS1#2 cells completely
443 lost the ability to generate metastasis in the lungs (Figure 6 K-N). Thus, we confirmed that
444 ASS1 expression is necessary for ccRCC cells to maintain their invasiveness *in vitro* and
445 colonize the lung *in vivo*.

446 **DISCUSSION**

447 Metabolic reprogramming is a hallmark of cancer (Hanahan and Weinberg, 2011; Pavlova and
448 Thompson, 2016) and in the recent years, there have been great efforts to map the metabolic
449 landscape of different tumor types (Pavlova and Thompson, 2016; Vander Heiden and
450 DeBerardinis, 2017). However, how cancer cells gain metabolic flexibility and what is its
451 biological impact through tumor evolution is still largely unknown.

452 In this study, we exploited a panel of cell lines, including renal cells, tumoral and their
453 metastatic derivatives, cultured for the first time under physiological nutrient conditions to
454 model the metabolic phenotype of renal cancer through its progression. Using this approach,
455 we identified BCAA catabolism as one of the metabolic pathways strongly reprogrammed in
456 renal cancer cells, whose transcriptional rewiring is sensitive to VHL restoration. Our findings
457 are consistent with other works showing that hypoxia suppresses the BCAA catabolism in
458 certain tissues (Wallace et al., 2018) but upregulates the expression of SLC7A5 and BCAT1
459 (Elorza et al., 2012; Onishi et al., 2019; Zhang et al., 2021) in different tumor types. By
460 combining metabolomic labelling experiments and a novel computational tool (ocEAn), we
461 studied the regulation of the BCAA catabolism in renal cancer cells, demonstrating that it
462 functions as a nitrogen reservoir for *de novo* biosynthesis of amino acids, especially aspartate
463 and asparagine through BCAT transamination. Strikingly, under nutrient deprivation, renal
464 cancer cells are capable to derive more than 60% of the aspartate nitrogen from BCAA
465 transamination. Moreover, BCAT inhibition impairs generation of intermediates of nucleotide
466 biosynthesis, confirming other reports showing that BCAT is important for the proliferation
467 (Mayers et al., 2016) and the survival (McBrayer et al., 2018) of cancer cells. This metabolic
468 rewiring is likely needed to compensate for the depletion of aspartate generated by the profound
469 mitochondrial defect observed in these cells. The epigenetic suppression of ASS1 could be an
470 additional metabolic strategy to spare aspartate and divert it to nucleotide biosynthesis in renal
471 cancer cells as previously shown (Rabinovich et al., 2015).

472 Our study showed that part of the nitrogen derived from BCAA is channeled into arginine
473 biosynthesis only in the metastatic renal cells. The integration between the BCAA catabolism
474 and urea cycle enzymes that emerged from our results bypassing the TCA cycle, was possible
475 because of a selective epigenetic re-activation of the argininosuccinate synthase (ASS1) in the
476 metastatic cells. This result was unexpected since it was recently shown that both ARG2 and
477 ASS1 are frequently lost in ccRCC through copy number aberrations (Ochocki et al., 2018).
478 Our findings showed that at least in a fraction of ccRCC, ASS1 is dynamically regulated and
479 that its re-expression is necessary for ccRCC to retain full metastatic potential *in vivo* and *in*

480 *vitro*. The evidence that *ASS1* is epigenetically silenced in other tumor types (Keshet et al.,
481 2018) and that arginine deprivation could trigger re-activation of *ASS1* in this condition
482 (Kremer et al., 2017) suggests that the re-expression of *ASS1* we observed in the metastatic
483 renal cells might be driven by changes in arginine availability, an event that might have
484 occurred at either the primary tumor level or at the metastatic site. This hypothesis is
485 corroborated by the evidence that the lung, one of the sites mostly colonized by ccRCC
486 metastases, shows a lower level of arginine, both at tissue and interstitial fluid level, compared
487 to the kidneys. Based on these results, a potential treatment of ccRCC patients with ADIPEG20,
488 currently in clinical trials in a range of other cancer types (e.g. lung, liver and pancreatic
489 cancers), should be carefully monitored since it might favor the selection of *ASS1*-proficient
490 and more aggressive subpopulations from the primary tumor.

491 In conclusion, we found that upon *VHL* loss, renal cancer cells activate a transcriptional
492 rewiring that compensates for the suppression of the mitochondrial respiration and consequent
493 depletion of aspartate through coordinated reprogramming of the BCAA catabolism and
494 suppression of *ASS1* to sustain proliferation (Figure 7). This mechanism is analogous to the
495 activation of alternative metabolic routes to cope with a mitochondrial defect shown in different
496 tumor types (Birsoy et al., 2015; Gaude et al., 2018; Mullen et al., 2011; Ryan et al., 2021;
497 Sullivan et al., 2015). Finally, through tumor progression, the reactivation of *ASS1*, which is
498 sensitive to the levels of arginine in the microenvironment and controlled by DNA methylation,
499 provides the metastatic renal cancer cells with the selective advantage to channel nitrogen from
500 BCAA to produce arginine (Figure 7). This novel metabolic flexibility might be important for
501 metastatic cells to survive in microenvironments with specific nutrient compositions and
502 effectively colonize distant tissues.

503 **Limitations of the study**

504 In this work, we have shown that *ASS1* is epigenetically regulated in ccRCC metastatic cells.
505 However, we have not investigated which specific transcription factor is responsible for its
506 transcriptional reactivation. We acknowledge that this is an essential aspect of *ASS1* biology
507 that deserves future investigations. Finally, although the patient's data supports the hypothesis
508 that *ASS1* expression is heterogeneous in ccRCC advanced tumors, we are aware that our
509 findings of the epigenetic regulation of *ASS1* in metastatic cells might be limited to the panel
510 of cell lines we used. Therefore, other regulatory mechanisms may regulate *ASS1* in renal
511 tumor progression, and, in different tumors, other metabolic adaptations independent from
512 *ASS1* may occur.

513 **STAR METHODS**

514 **Cell culture**

515 The human ccRCC 786-O and OS-RC-2 cells were obtained from J. Massaguè (MSKCC, NY-
516 US) in 2014. Metastatic derivatives 786-M1A, 786-M2A and OS-LM1 have been previously
517 described (Vanharanta et al., 2013). HK2 cells were a gift from the laboratory of Prof. Eamonn
518 Maher (University of Cambridge, UK). All cells were authenticated by short tandem repeat
519 (STR) and routinely checked for mycoplasma contamination and cultured in complete Plasmix
520 medium prepared as described before (Vande Voorde et al., 2019) or RPMI (Sigma Aldrich)
521 supplemented with 10% fetal bovine serum (FBS, Gibco-Thermo Scientific). All cells were
522 cultured and passaged for at least 3 weeks in an incubator at 37°C with 5% CO₂, to adapt to the
523 Plasmix composition before starting to perform experiments. Counting for plating and volume
524 measurement were obtained using CASY cell counter (Omni Life Sciences). Briefly, cells were
525 washed in PBS once, then detached using trypsin-EDTA 0.05% (Gibco, Thermo Scientific).

526 **Cell growth**

527 Cell proliferation was analyzed using the Incucyte SX5 by means of phase contrast sharpness
528 for 4 days or through sulphorhodamine B staining. Briefly, 2×10^4 cells were plated onto 12-
529 well plates (3 replicates/experimental condition for each cell line) and at each time point the
530 cells were washed in PBS and incubated at 4°C with 1% TCA solution. After two washes in
531 water and once the plates were dry, the wells were treated with 0.057% of Sulforhodamine B
532 (SRB) in acetic acid for 1h at room temperature. After two additional washes in 1% acetic acid
533 solution, plates were left to dry. To quantify the differences of the staining, the SRB was
534 dissolved in 10mM Tris solution and quantified using TECAN spectrophotometer reading the
535 absorbance at 560 nm.

536 **VHL-re-expression in ccRCC cells**

537 786-O and 786-M1A \pm VHL cells were previously generated (Rodrigues et al., 2018). For
538 comparison, cells transduced with empty vector (EV) were used. All cells were selected and
539 then stably grown in RPMI with $2\mu\text{g/ml}$ puromycin (Gibco, Thermo-Scientific).

540 **LC-MS Metabolomics**

541 Steady-state metabolomics

542 For steady-state metabolomics, 2×10^5 cells were plated the day before onto 6-well plate (5 or
543 6 replicates for each cell type) and extracted the day after. The experiment was repeated 3 times
544 (N=3). Before extraction, cells were counted using CASY cell counter (Omni Life Sciences)
545 using a separate counting plate. After that, cells were washed at room temperature with PBS
546 twice and then kept on cold bath with dry ice and methanol. Metabolite extraction buffer (MEB)
547 was added to each well following the proportion 1×10^6 cells/1 ml of buffer. After a couple of
548 minutes, the plates were moved to the -80°C freezer and kept overnight. The following day, the
549 extracts were scraped and mixed at 4°C for 10 min. After final centrifugation at max speed for
550 10 min at 4°C , the supernatants were transferred into LC-MS vials.

551 Tracing experiments

552 2×10^5 cells were plated onto 6-well plate (5 or 6 replicates for each cell type). The day after,
553 the medium was replaced with fresh one containing the labelled isotopologue metabolite. For
554 $^{13}\text{C}_6$ L-Leucine and $^{13}\text{C}_6$ L-Isoleucine (obtained from Cambridge Isotopes Laboratories)
555 tracing experiment in Plasmax, cells were incubated for the indicated short time points or 43h.
556 For ^{15}N L-Leucine and Isoleucine (Sigma Aldrich) tracing for 27h. The labelling experiment
557 with ^{15}N L-Leucine in nutrient-deprived condition was conducted for 24h in EBSS containing
558 2.5% FBS and $380\mu\text{M}$ of ^{15}N L-Leucine (Sigma Aldrich).

559 Liquid chromatography coupled to Mass Spectrometry (LC-MS) analysis

560 LC-MS was performed on a Dionex Ultimate 3000 LC system coupled to a Q Exactive mass
561 spectrometer (Thermo Scientific). A Sequant ZIC-pHILIC column (2.1 x 150 mm, 5 μM)
562 (Merck) was used to separate metabolites. Mobile phases consisted of 20 mM $(\text{NH}_4)_2\text{CO}_3$,
563 0.05% NH_4OH in H_2O (Buffer A) and acetonitrile (Buffer B). The flow rate was 200 $\mu\text{l/min}$
564 with a gradient starting at 80% (A) decreasing to 20% (A) over 17 minutes followed by washing
565 and re-equilibration steps. Ionization was achieved in a HESI probe connected to the Q
566 Exactive which scanned a mass range between 50 and 750 m/z with polarity switching. The
567 acquired spectra were analyzed using Quan Browser software (Thermo Scientific). For tracing
568 experiments, after calculating the theoretical masses of $^{13}\text{C}/^{15}\text{N}$ isotopes, the molecules were
569 searched within a 5-ppm tolerance. Finally, the peak was integrated when the difference of

570 retention time from the [U-12C] monoisotopic mass in the same chromatogram was lower than
571 1%. Correction for natural abundances was performed using the AccuCor algorithm
572 (<https://github.com/lparsons/accucor>).

573 Mouse Tissue and interstitial fluid analysis

574 Mice of a hybrid C57BL/6J;129/SvJ background were bred and maintained under pathogen
575 free conditions at the MRC ARES Breeding Unit (Cambridge, UK). Animals of about 12 weeks
576 of age were killed by neck dislocation and blood and tissues were speedily collected and
577 processed for further analysis. Blood was recovered from the aorta, transferred to EDTA tubes
578 (MiniCollect, Greiner Bio-One, 450531) and stored at -80°C. The tissue samples were split
579 into two: one snap frozen in liquid nitrogen and stored at -80°C until further processing, the
580 second was used for interstitial fluid extraction using a protocol adapted from Sullivan et al.
581 2019. After the tissues were weighed, they were rinsed in room temperature saline (150 mM
582 NaCl) and blotted on filter paper (VWR, Radnor, PA, 28298–020). We collected the hearts,
583 livers, kidneys, and lungs from 8 wild-type mice and homogenized a piece of the tissue in
584 metabolite extraction buffer using the proportion 25 µl/mg of buffer with Precellys Lysing
585 tubes (Bertin Instruments). After that, extracts were kept in the freezer overnight and the
586 following day centrifuged twice at max speed at 4°C to remove the protein precipitates. Equal
587 volume of supernatants was spiked in with ¹³C arginine (Cambridge Isotopes) for quantification
588 of arginine content. For extraction of the tissue interstitial fluid, we adapted the protocol from
589 Sullivan et al.2019. Briefly, the organ was washed in saline solution and then a portion was
590 centrifuged at for 10 min at 4°C at 106 x g using 20 µm nylon filters (Spectrum Labs, Waltham,
591 MA, 148134) affixed on top of 2 ml Eppendorf tubes. 1µl of the eluate was extracted in 45µl
592 of extraction buffer and frozen overnight. The following day, all extracted were centrifuged
593 twice at max speed at 4°C to remove the protein precipitates. Supernatants were finally spiked
594 in with ¹³C arginine (Cambridge Isotopes) for arginine quantification.

595 Patient samples

596 For the metabolic comparison in Figure S2 we used the data we generated and published in
597 Dugourd et al.2021 from renal tumors and matched healthy tissue. The local ethics committee
598 of the University Hospital RWTH Aachen approved all human tissue protocols for this study
599 (EK-016/17). The study was performed according to the declaration of Helsinki. All patients
600 gave informed consent. Kidney tissues were sampled by the surgeon from normal and tumor
601 regions. The tissue was snap-frozen on dry-ice or placed in prechilled University of Wisconsin
602 solution (#BTLBUW, Bridge to Life Ltd., Columbia, U.S.) and transported on ice.

603 The samples used for the metabolomics analysis in Figure S6 were generated using frozen
604 tissue from surgically resected clear cell renal cell carcinoma samples that were sourced from
605 an ongoing ethically approved study of biomarkers in urological disease (Ethics 03/018, CI
606 V.J.G). From this study, we selected 18 primary tumors samples collected from patients treated
607 from 2015-2017 and presenting with metastatic disease. Before processing the samples, whole
608 frozen tissue areas of tumor were identified and marked by a uro-pathologist (A.Y.W). After
609 that, samples were extracted for LC-MS analysis as described before (Sciacovelli et al., 2016).

610 Consumption-release (CoRe) experiments

611 1.5×10^5 cells were seeded onto a 6-well plate and experiment carried as previously described
612 (Goncalves et al., 2018) . Values represent the mean of 5 independent cultures \pm S.D. and are

613 relative to the metabolite abundance normalized to biomass dry weight generated (dW) in 24h
614 after medium background subtraction.

615 **RNA sequencing**

616 4×10^5 cells were plated onto 5 replicate 6-cm dishes the day before the extraction. RNA
617 isolation was carried using RNeasy kit (Qiagen) following manufacturer's suggestions and
618 eluted RNA was purified using RNA Clean & Concentrator Kits (Zymo Research). RNA-seq
619 samples libraries were prepared using TruSeq Stranded mRNA (Illumina) following the
620 manufacturer's description. For the sequencing, the NextSeq 75 cycle high output kit (Illumina)
621 was used and samples spiked in with 1% PhiX. The samples were run using NextSeq 500
622 sequencer (Illumina).

623 Analysis

624 Counts were generated from the read files using the Rsubread package with the hg38 genome
625 build. Gene that had less than 50 counts per sample on average were filtered out. Then, 0 count
626 values were scaled up to 0.5 (as done in the voom normalization procedure of the limma R
627 package) and then log₂ transformed and normalized with the VSN R package. Differential
628 analysis was then performed using the limma R package.

629 Transcription factor activity from RNA-seq

630 TF activities were estimated from the limma t-values as gene-level statistics, with the TF-target
631 regulons from the dorothea v1.3.0 R package and the viper algorithm. Dorothea regulons were
632 filtered to include TF-target interactions of confidence A, B, C and D. Viper was run with a
633 minimum regulon size of 5 and eset filter set to FALSE. The resulting TF activity scores
634 roughly represent how extreme is the average deregulation of a set of target genes of a given
635 TF, compared to the rest of genes.

636 **Proteomics analysis**

637 Sample preparation

638 Cell pellets were lysed, reduced and alkylated in 100 μ l of 6M Gu-HCl, 200 mM Tris-HCl pH
639 8.5, 1 mM TCEP, 1.5 mM Chloractamide by probe sonication and heating to 95°C for 5 min.
640 Protein concentration was measured by a Bradford assay and initially digested with LysC
641 (Wako) with an enzyme to substrate ratio of 1/200 for 4 h at 37 °C. Subsequently, the samples
642 were diluted 10fold with water and digested with porcine trypsin (Promega) at 37 °C overnight.
643 Samples were acidified to 1% TFA, cleared by centrifugation (16,000 g at RT) and
644 approximately 20 μ g of the sample was desalted using a Stage-tip. Eluted peptides were
645 lyophilized, resuspended in 0.1% TFA/water and the peptide concentration was measured by
646 A280 on a nanodrop instrument (Thermo). The sample was diluted to 1 μ g/ 5 μ l for subsequent
647 analysis.

648 Mass spectrometry analysis

649 The tryptic peptides were analyzed on a Fusion Lumos mass spectrometer connected to an
650 Ultimate Ultra3000 chromatography system (both Thermo Scientific, Germany) incorporating
651 an autosampler. 5 μ L of the tryptic peptides, for each sample, was loaded on a homemade
652 column (250 mm length, 75 μ m inside diameter [i.d.]) packed with 1.8 μ m uChrom
653 (nanoLCMS Solutions) and separated by an increasing acetonitrile gradient, using a 150-min
654 reverse-phase gradient (from 3%–40% Acetonitrile) at a flow rate of 400 nL/min. The mass
655 spectrometer was operated in positive ion mode with a capillary temperature of 220 °C, with a
656 potential of 2000 V applied to the column. Data were acquired with the mass spectrometer

657 operating in automatic data-dependent switching mode, with MS resolution of 240k, with a
658 cycle time of 1 s and MS/MS HCD fragmentation/analysis performed in the ion trap. Mass
659 spectra were analyzed using the MaxQuant Software package in biological triplicate. Label-
660 free quantification was performed using MaxQuant. All the samples were analyzed as
661 biological replicates.

662 Data analysis

663 Data were analyzed using the MaxQuant software package. Raw data files were searched
664 against a human database (Uniprot Homo sapiens), using a mass accuracy of 4.5 ppm and 0.01
665 false discovery rate (FDR) at both peptide and protein level. Every single file was considered
666 as separate in the experimental design; the replicates of each condition were grouped for the
667 subsequent statistical analysis. Carbamidomethylation was specified as fixed modification
668 while methionine oxidation and acetylation of protein N-termini were specified as variable.
669 Subsequently, missing values were replaced by a normal distribution (1.8π shifted with a
670 distribution of 0.3π) in order to allow the following statistical analysis. Results were cleaned
671 for reverse and contaminants and a list of significant changes was determined based on average
672 ratio and t-test. Intensities were then normalized using the VSN package and differential
673 analysis was performed with limma (same as for the RNA data). Gene set enrichment analysis
674 was performed using the FGSEA package and the kegg pathway ontology (obtained from
675 mSigDB).

676 ***In vivo* metastatic assay**

677 All animal experiments were performed in accordance with protocols approved by the Home
678 Office (UK) and the University of Cambridge ethics committee (PPL PFCB122AA). For
679 experimental lung metastasis assays, 300000 cells were resuspended in 100 μ L PBS and
680 inoculated in the lateral tail vein of 7 weeks old female NOD/SCID mice obtained from Charles
681 River Laboratories. Metastatic colonization was monitored by IVIS bioluminescence imaging
682 (PerkinElmer). At the experimental endpoint lungs were harvested for immunohistochemistry.

683 **Immuno-histochemistry staining (IHC)**

684 Lungs were collected and fixed overnight with neutral formalin 4% and washed with PBS, 50%
685 ethanol, and 70% ethanol for 15 minutes each. Lungs were embedded in paraffin, sectioned,
686 and stained with H&E by the human research tissue bank and histopathology research support
687 group from the Cambridge University Hospitals-NHS Foundation. Human Vimentin staining
688 (Cell signaling #5741 1:100) was carried out using the Bond Max (Leica) using Bon polymer
689 Refine Detection reagents (Leica) according to manufacturer's protocol (IHC protocol F). Two
690 different lung sections were vimentin-stained and imaged using Wide Field Zeiss Axio
691 Observer 7 microscope (Zeiss).

692 **Oxygen consumption rate and extracellular acidification rate measurements**

693 Cellular respiration (Oxygen consumption rate, OCR) was measured using the real-time flux
694 analyzer XF-24e Seahorse (Agilent) as described before (Sciacovelli et al., 2016). Briefly,
695 6×10^4 cells were plated onto the instrument cell plate 24h before the experiment in complete
696 Plasmax medium or RPMI (at least 4 replicate wells for each cell line). The following day, the
697 medium was replaced with fresh Plasmax supplemented with 25mM HEPES (Sigma-Aldrich)
698 to balance pH changes without any pre-incubation or with Agilent Seahorse XF RPMI with the
699 addition of glucose, pyruvate and glutamine at the concentration present in normal RPMI and
700 pre-incubated for 30 min at 37C. Cells were treated with 1 μ M Oligomycin, 4 μ M FCCP and
701 1 μ M Antimycin A (all drugs were purchased from Sigma-Aldrich).

702 **TCGA KIRC transcriptomic analysis**

703 KIRC RNAseq counts were downloaded from the TCGA portal. Data were normalized in
704 several steps. First, counts were \log_2 transformed. After visual inspection of the data
705 distribution, any \log_2 count values lower than 7.5 were converted to missing values (NAs).
706 Samples containing more than 49000 NAs were removed. Then, genes with 350 or more
707 missing values across samples were excluded. This yielded a clean data matrix of 593 samples
708 and 13452 genes. The data was converted back to original count values so that VSN
709 normalization procedure could be applied.

710 Groups were first defined as early-stage tumors (stage I and II) and late-stage tumors (stage III
711 and IV). ASS1 expression distribution was visually inspected in each group. Then the late-
712 stage tumor group was split into two subgroups based on ASS1 expression. We used Gaussian
713 mixture modelling with the mclust package to model ASS1 expression across late-stage tumor
714 samples with two Gaussian distributions. This allowed us to define a group of low expression
715 of ASS1 (177 samples) and high expression of ASS1 (18 samples, with a probability of sample
716 belonging to a given distribution of 50%). Limma was used to perform differential analysis
717 between late-stage tumors that express high/low ASS1 and early-stage tumors. FGSEA (nperm
718 = 1000) was used with the resulting limma t-values and KEGG pathway collection (obtained
719 from msigdb) to perform a pathway enrichment analysis.

720 **Metabolomic enrichment analysis using ocEAn**

721 Pre-processing of metabolomic data

722 Steady-state metabolomics

723 Three sets of metabolomic data relative to cells stably cultured in Plasmax were combined and
724 the batch effect was removed with the removeBatchEffect function of limma (using a linear
725 model to regress out the batch effect). We compared both 786-O and 786-M1A to HK2 and
726 786-M1A vs 786-O using limma differential analysis and t-values relative to significant
727 differences were calculated for each metabolite.

728 Pre-processing of recon2 reaction network

729 To run OcEAn, we first generated a list of metabolites associated with each enzyme. This
730 information was extracted from the metabolic reaction network, indicating which metabolites
731 are downstream or upstream of each reaction. The quality of the metabolic reaction network
732 used to generate the set is of prime importance, as the choice of an adequate prior-knowledge
733 source usually impacts the quality of footprint-based activity estimations the most. We used a
734 reduced manually curated and thermodynamically proofed version of the Recon2 human
735 metabolic reaction network to identify metabolites associated with each reaction. The
736 thermodynamic proofing was performed using the TFBA algorithm to exclude reaction
737 directions that were not thermodynamically feasible. To compute the relative position of the
738 metabolites relative to the enzymes, we first filtered out accessory elements of the reaction
739 network such as cofactors and over-promiscuous metabolites (over-promiscuous metabolites
740 are metabolites that are used as reactants by >100reactions). Metabolites classified as cofactors
741 and nucleotides according to the KEGG BRITE classification were removed, as well as CO₂,
742 ITP, IDP, NADH and all metabolites composed of less than four atoms. This procedure filtered
743 out 100 metabolites, bringing the number of metabolites in the reaction network from 421 to
744 321.

745 Convert redHuman network into an enzyme-metabolite distance map The gene-reaction rules
746 ("AND" and "OR" which contains the information about which genes are required for a

747 reaction to occur) of the metabolic reaction network were used to associate reactants and
748 products with the corresponding enzymes of each reaction. When multiple enzymes were
749 associated with a reaction with an "AND" rule, they were combined as a single entity
750 representing an enzymatic complex. Then, reactants were connected to corresponding
751 enzymatic complexes or enzymes by writing them as rows of a Simple Interaction Format (SIF)
752 table in the following form: enzyme; 1; product. In this way, each row of the SIF table
753 represents either activation of the enzyme by the reactant (i.e. the necessity of the presence of
754 the reactant for the enzyme to catalyze its reaction) or activation of the product by an enzyme
755 (i.e. the product presence is dependent on the activity of its corresponding enzyme). The
756 resulting network allows to easily follow paths connecting metabolic enzymes with distant
757 metabolites and can be converted to an enzyme-metabolite graph (using igraph package in R).
758 The paths have to conserve the compartment information of metabolites and reactions, thus
759 enzymes and metabolites are duplicated and uniquely identified based on each reaction they
760 are involved in. Finally, since the same enzyme catalyzes the transformation of different
761 reactions (with variations of reactants and products), each reaction linked to a metabolic
762 enzyme was uniquely identified (Table 1). This level of resolution guarantees the correct
763 tracking of a series of reactions from a metabolite to another without having incoherent jumps
764 between metabolites catalyzed by the same enzyme.

765 The enzyme-metabolite graph was used to find the shortest path between each metabolic
766 enzyme and all the other metabolites of the network. This is done first following the normal
767 reaction fluxes (to connect enzymes with direct and indirect metabolic products) and then
768 following the reversed fluxes (to connect enzymes with direct and indirect metabolic reactants).
769 This yields a "reaction network forest", where each tree has a root corresponding to a specific
770 metabolic enzyme, and branches represent the metabolites that can be reached from this
771 enzyme, following normal or reverse reaction flux directions. Thus, each tree allows us to know
772 if a given metabolite is upstream or downstream of a specific reaction and how many reaction
773 steps separate them. The next step was associating each enzyme and all metabolites of the
774 network with weights, representing the minimum distance of metabolites relative to enzymes,
775 and a sign representing whether each metabolite is upstream (-1 to 0) or downstream (0 to 1)
776 of a given enzyme. To compute a weight, we used a function that progressively decreases the
777 weight value with the distance in the network. The weight value starts at 1 for direct reactant
778 and products of a given enzyme and decreases in a stepwise manner ($x_{i+1} = x_i * \text{penalty}$,
779 with $x_0 = 1$ and dissipation parameter ranging between 0 and 1), for each reaction step
780 separating the given metabolite from a given enzyme. In this study, we used a dissipation
781 parameter of 0.8, which represents a drop of the weight of a given metabolite to a given enzyme
782 of 20% per step in the reaction network. This value is arbitrary and was chosen because it
783 allowed us to generate visually interpretable metabolic enzyme profiles. Since many cycles are
784 present in the metabolic reaction network, metabolites are usually both upstream and
785 downstream of different enzymes. To obtain a weight that represents the actual relative position
786 of a metabolite relative to a given enzyme, the upstream and downstream weight of each
787 metabolite-enzyme association were averaged.

788 **RNA extraction and real-time PCR**

789 2.5×10^5 cells were plated onto a 6-well plate. The day after, cells were washed in PBS and then
790 RNA was extracted using RNeasy kit (Qiagen) following the manufacturer's protocol. RNA
791 was eluted in water and then quantified using Nanodrop (Thermo Fisher). 500 ng of RNA was
792 reverse-transcribed using Quantitect Reverse Transcription kit. For real-time qPCR, cDNA
793 was run using Taqman assay primers (Thermo Scientific) and Taqman Fast 2X master mix
794 (Thermo Scientific). TATA-Box Binding Protein (*TBP*) was used as the endogenous control.

795 Data and biological replicates were analyzed using Expression Suite (Thermo Scientific).
796 Results were obtained from three independent experiments and presented as Relative
797 quantification (RQ), with RQ max and RQ min calculated using SD1 algorithm. p-values were
798 calculated by Expression Suite software.

799 **Treatment of cells with BCAT inhibitor**

800 2×10^4 cells were plated onto 6-well plates (5 replicates/experimental condition for each cell
801 line) and incubated with either the appropriate vehicle or 100 μ M BCATI2, (ApexBio)
802 dissolved in DMSO for 22h at 37°C with 5% CO₂ before the metabolite extraction.

803 **Treatment of cells with DNA methylation inhibitor 5-azacitidine (5AC)**

804 1×10^5 786-O and OS-RC-2 cells were plated onto 6-well plates and incubated with either the
805 appropriate vehicle or the inhibitor 5-Azacytidine, (Sigma-Aldrich) dissolved in DMSO at
806 200nM concentration for 72h 37°C with 5% CO₂. The medium was replaced every day with
807 fresh one containing either vehicle or the inhibitor. After 96h, cells were washed in PBS and
808 RNA extracted as described above for real-time qPCR. The experiment was repeated three
809 times (N=3).

810 **Treatment of cells with ADIPEG20**

811 3×10^4 cells were plated onto 24-well plates (4 replicates/conditions). The day after, pegylated
812 arginine deiminase (ADIPEG20, Design Rx Pharmaceutical, US) was added at 115 ng/ml
813 concentration for 72h. Then, cells were fixed with 1%TCA solution at 4C for 10 min. After the
814 plate was washed twice in water and dried, cells were colored using SRB staining solution
815 (0.057% in acetic acid) for 1h at room temperature. After two washes in 1% acetic acid solution
816 and once dry, the SRB staining was dissolved in 10mM Tris-EDTA solution and absorbance
817 quantified using TECAN spectrophotometer at 560 nm. The experiment was repeated 4 times
818 (N=4). For chronic treatment, 786-O cells were plated (5×10^5) onto a T25 flask and treated
819 with ADIPEG20 57.5 ng/ml for 4 weeks. Medium was replaced with fresh ADIPEG20 every
820 3 days.

821 **Short hairpin RNA (shRNA) interference experiments**

822 786-M1A were infected with lentiviral particles which were a gift from Ayelet Erez's
823 laboratory. The virus was generated transfecting HEK293T cells with psPAX, pVSVG vectors,
824 which encode for the virus assembly, and pLKO shGFP, shASS1 (Catalog #: RHS4533-
825 EG445, GE Healthcare, Dharmacon). Cells were incubated with a medium containing the
826 lentiviral particles for 24h. After lentiviral transduction, cells were selected with puromycin
827 2ug/ml for 48h and then kept at 1ug/ml for downstream experiments.

828 **Invasive growth assay**

829 The invasive growth assay was performed as described previously (Torrano et al., 2016;
830 Valcarcel-Jimenez et al., 2019). Briefly, cells (1000 cells/drop) were maintained in drops (25
831 μ L/drop) with Plasmax and 6% methylcellulose (Sigma M0387) on the cover of a 100- mm
832 culture plate. Drops were incubated at 37°C and 5% CO₂ for 72 hours. Once formed, spheroids
833 were collected, resuspended in collagen I solution (Advanced BioMatrix PureCol), and added
834 to 24-well plates. After 4 hours, Plasmax medium was then added on top of the well and day 0
835 pictures were taken. Increase in spheroid area was monitored taking pictures with Incucyte SX5
836 for 48 hours. For invasive growth quantification, an increase in the area occupied by the
837 spheroids between day 0 and day 2 was calculated using Fiji software.

838 **DNA Methylation analysis**

839 DNA samples (10ng/μl, 500ng total) were sheared using the S220 Focused-ultrasonicator
840 (Covaris) to generate dsDNA fragments. The D1000 ScreenTape System (Agilent) was used
841 to ensure >60% of DNA fragments were between 100 and 300bp long, with a mean fragment
842 size of 180-200bp. The methylation analysis was performed using the TruSeq Methyl Capture
843 EPIC Library Preparation Kit (Illumina), using the manufacturer's protocol. Twelve samples
844 were pooled for sequencing on the HiSeq4000 Illumina Sequencing platform (single end 150bp
845 read) using two lanes per library pool. Technical replicates were performed for cell line data to
846 assess assay reproducibility ($R^2=0.97$). Quality control (QC) was performed using FastQC and
847 MultiQC. Reads were trimmed (TrimGalore v0.4.4) using standard parameters, aligned to the
848 bisulfite converted human reference genome (GRCh38/hg38) and methylation calling was
849 performed using the Bismark suite (v0.22.1). The position of the CpG island (hg38-
850 chr9:130444478-130445423) overlapping with the TSS of *ASS1* (GRCh38 chr9:130444200-
851 13044780) was obtained from *Ensembl*.

852 **Chromatin immunoprecipitation and sequencing (ChIP-seq)**

853 ChIP experiments were generated and described previously (Rodrigues et al., 2018).

854 **Protein lysates and western blot**

855 6×10^5 cells were plated onto 6-cm dishes. The day after, cells were washed in PBS and then
856 lysed on ice with RIPA buffer (150mM NaCl, 1%NP-40, Sodium deoxycholate (DOC) 0.5%,
857 sodium dodecyl phosphate (SDS) 0.1%, 25mM Tris) supplemented with protease and
858 phosphatase inhibitors (Protease inhibitor cocktail, Phosphatase inhibitor cocktail 2/3, Sigma-
859 Aldrich) for 2 minutes. Cells extracts were scraped and then sonicated for 5 min (30 sec on, 30
860 sec off) using Bioruptor sonicator (Diagenode) and the protein content measured using BCA
861 kit (Pierce) following the manufacturer's instructions. Absorbance was read using TECAN
862 spectrophotometer at 562 nm. 30-50 μg of proteins were then heated at 70°C for 10 minutes in
863 Bolt Loading buffer 1X (Thermo Scientific) containing 4% β-mercaptoethanol. Then, the
864 samples were loaded into 4-12% Bis-Tris Bolt gel and run at 160V constant for 1h in Bolt MES
865 1X running buffer (Thermo Scientific). Dry transfer of the proteins to a nitrocellulose
866 membrane was done using IBLOT2 (Thermo Scientific) for 12 minutes at 20V. Membranes
867 were incubated in blocking buffer for 1h (either 5% BSA or 5% milk in TBS 1X +0.01 %
868 Tween-20, TBST 1X). Primary antibodies were incubated in blocking buffer ON at 4°C.
869 Calnexin antibody was purchased from Abcam (ab22595), BCAT1 from Cell Signalling
870 (#12822), ASS1 from Abcam (ab124465), BCDHA from Cell Signalling (#90198), and
871 pSer293 BCDHA from Cell Signalling (#40368) The day after, the membranes were washed
872 three times in TBST 1X and then secondary antibodies (conjugated with 680 or 800 nm
873 fluorophores, Li-Cor) incubated for 1h at room temperature at 1:2000 dilution in blocking
874 buffer. Images were acquired using Image Studio lite 5.2 (Li-Cor) on Odyssey CLx instrument
875 (Li-Cor).

876 **Graphs and statistical analysis**

877 Graphs were generated using Graphpad Prism 8. The experiments were performed 3 times
878 unless differently specified. The statistical analysis was performed using Prism software and
879 performing either unpaired/paired t-test or one-way ANOVA with multiple comparisons. For
880 real-time qPCR, the statistical analysis was performed using Expression Suite software using
881 SD algorithm on 3 independent experiments.

882 **Code and data availability**

883 ocEAn package is available at: <https://github.com/saezlab/ocean>

884 All data and script for the analysis are available at:
885 https://github.com/saezlab/Sciacovelli_Dugourd_2021

886 Whole network result based on the metabolomics data is available at:
887 <https://sciacovelli2021.omnipathdb.org>

888 **Acknowledgements**

889 We thank Dr Alexandria Karcianas and Dr Julien Bauer (Cambridge Genomic Services,
890 Department of Pathology, University of Cambridge) for the RNA-seq library preparation and
891 sequencing; the human research tissue bank and histopathology research support group from
892 the Cambridge University Hospitals-NHS Foundation for the lung tissue processing. We thank
893 Saverio Tardito for providing us with the Plasmax medium and for the guidance during the
894 preparation of the medium formulation in house. We thank Denes Turei for helping set up the
895 interactive metabolic networks online. We thank all the members of Frezza's laboratory for
896 critical reading and discussion of the manuscript. We thank Sivan Pinto for generating the
897 shASS1 plasmids. A.E is supported by research grants from the European Research Council
898 (ERC 818943), and from the Israel Science Foundation (860/18). A.E received additional
899 support from the Moross Integrated Cancer Center, Koret foundation, Blumberg family, and
900 from Manya and Adolph Zarovinsky. We acknowledge funding by German Federal Ministry
901 of Education and Research (Bundesministerium für Bildung und Forschung BMBF)
902 MSCoreSys research initiative research core SMART-CARE (031L0212A). A.D was
903 supported by the European Union's Horizon 2020 research and innovation program (675585
904 Marie-Curie ITN "SymBioSys"). G.D.S is supported The Mark Foundation for Cancer
905 Research, the Cancer Research UK Cambridge Centre [C9685/A25177] and NIHR Cambridge
906 Biomedical Research Centre (BRC-1215-20014). The views expressed are those of G.D.S and
907 not necessarily those of the NIHR or the Department of Health and Social Care. A.Y.W is
908 supported by the NIHR Cambridge Biomedical Research Centre and the Urological
909 Malignancies Programme, funded by CRUK UK Major Centre Award C9685/A25117. L.V.J
910 is supported by a FEBS Long-term fellowship. M.S and C.F are supported by the MRC Core
911 award grant MRC_MC_UU_12022/6.

912 **Author contributions**

913 M.S and C.F conceptualized the study. M.S designed and performed the majority of the
914 experiments, interpreted the data and coordinated the research. M.S prepared the figures and
915 wrote the manuscript with assistance from all other authors. A.D generated the computational
916 tool ocEAn with the help of J.S.R, C.L, M.M.B, V.H and performed all bioinformatic analyses.
917 L.V.J generated the data relative to the silencing of ASS1 and performed the *in vivo*
918 experiments with the help of V.C and S.V. M.Y, E.N, A.S.H.C and L.T ran and analyzed the
919 metabolomics samples. T.Y and V.R.Z collected the mouse tissue and extracted the samples
920 for measurement of arginine in mouse tissue and interstitial fluids. P.R generated ccRCC cells
921 expressing wt-VHL and performed the ChIP-seq analysis relative to H3k27ac. D.R provided
922 advice and helped with editing of the manuscript. C.S, S.H.R and C.M performed the EPIC
923 methylation analysis and analyzed the data. A.E provided reagents, advice and helped with
924 editing of the manuscript. A.v. K prepared the proteomic samples and analyzed the data. V.G,
925 G.D.S, C.K and R.K collected the ccRCC patients used in the study. A.Y.W performed the
926 histopathological analysis of the patients' tumors. C.F edited the manuscript and oversaw the
927 research program.

928 **Declaration of interests**

929 G.D.S has received educational grants from Pfizer, AstraZeneca and Intuitive Surgical;
930 consultancy fees from Pfizer, Merck, EUSA Pharma and CMR Surgical; Travel expenses from
931 Pfizer and Speaker fees from Pfizer.

932 **Figure legends**

933
934 **Figure 1. Branched-chain amino acids catabolism is suppressed in KIRC.** **A)** Dot plot
935 showing the enriched pathways ranked by significance in KIRC tumors compared to renal
936 healthy tissue obtained through GSEA analysis of RNA-seq data from TCGA. The dot size
937 represents the significance expressed as $-\log_{10}(\text{p-value})$. red dots=upregulated pathways, purple
938 dots= downregulated pathways. NES= normalized enrichment score. **B)** Volcano plot showing
939 the differential expression of genes that belong to KEGG ‘Valine leucine and isoleucine
940 degradation’ signature in KIRC tumors compared to renal healthy tissue. FC= fold change;
941 red=upregulated genes, blue=downregulated genes. **C)** Dot plot of the differentially enriched
942 pathways in KIRC tumors comparing stage III/IV vs stage I/II. Pathways, ranked by
943 significance, are obtained through GSEA analysis of TCGA RNA-seq data. The dot size
944 represents the absolute value of the normalized enrichment score ($\text{abs}(\text{NES})$). Red
945 dots=upregulated pathways, purple dots=downregulated pathways. **D)** Overall survival of
946 KIRC patients obtained through GEPIA, based on gene expression of KEGG ‘Valine, leucine
947 and isoleucine degradation’ signature. Cut-off used for high/low groups was 50% and p-value
948 displayed as $-\log_{\text{rank}}(\text{p-value})$. The dotted line refers to the survival with a confidence interval
949 (CI) of 95%. n=number of samples compared; HR=hazard ratio based on the Cox PH model.
950 KIRC=Renal clear cell carcinoma.

951
952 **Figure 2. BCAA catabolism regulation in a cellular model system for renal cancer**
953 **progression.** **A)** Schematics depicting the cell lines used in the study. HK2 cells were isolated
954 from normal renal tissue, 786-O, OS-RC-2, RFX-631 from primary clear cell renal cell
955 carcinomas (ccRCC) and the metastatic 786-M1A, 786-M2A, and OS-LM1 were derived from
956 lung metastases after injection in the mice tail vein of 786-O and OS-RC-2 respectively. **B)**
957 Dot plot of the enriched pathways ranked by significance obtained through GSEA from
958 proteomic data. Green dots are relative to 786-O vs HK2 comparison, orange to 786-M1A vs
959 HK2, 786-M1A vs 786-O dots are blue **(C).** All cells were stably grown in Plasmax medium.
960 Dot size is proportional to $-\log_{10}(\text{adj-p-value})$. NES= normalized enrichment score. **D)** Dot plot
961 showing the differential abundance of the indicated intracellular metabolites in the comparisons
962 786-O vs HK2 (green), 786-M1A vs HK2 (orange), and 786-M1A vs 786-O (blue, **E)** ranked
963 by significance. Data were normalized to total ion count and generated from N=3 experiments
964 while the ranking was based on t-values. The dimension of the dots is based on the $\text{abs } t$ -values.
965 **F)** Simplified schematic of the BCAA catabolism. Leucine and isoleucine are imported within
966 the cells through a specific solute carrier system SLC7A5/SLC3A2 then converted in branched-
967 chain keto acids (BCKAs) through BCAT1/2 transamination and subsequently oxidized by
968 BCKDH complex, whose activity is inhibited by BCKDK-dependent phosphorylation on
969 Ser293 into Acyl-CoAs. The derived metabolites C5 and C3-carnitines are measured as readout
970 of isovaleryl-CoA and propionyl-CoA respectively. Acyl-CoAs are further catabolized through
971 a series of reactions similar to fatty acids oxidation which are catalyzed by IVD, ACADS,
972 ACADSB, ACADM, MMUT. Final degradation of the amino acids generates CO₂ and carbons
973 to feed the TCA cycle. Metabolites indicated in orange circles are measured by LC-MS. Red
974 circles= metabolites from leucine catabolism, black circles= metabolites derived from
975 isoleucine, blue circles=metabolites derived from valine. SLC7A5=Solute Carrier Family 7
976 Member 5; SLC3A2=Solute Carrier Family 3 Member 2; BCAT1/2= Branched Chain Amino
977 Acid Transaminase 1/2; BCKDH= Branched Chain Keto Acid Dehydrogenase complex

978 BCKAs= branched-chain keto acids; BCDK= Branched Chain Keto Acid Dehydrogenase
979 Kinase; IVD=Isovaleryl-CoA Dehydrogenase; ACADS=Acyl-CoA Dehydrogenase Short
980 Chain; ACADSB= Acyl-CoA Dehydrogenase Short/Branched Chain; ACADM=Acyl-CoA
981 Dehydrogenase Medium Chain; MMUT=Methylmalonyl-CoA Mutase.

982

983 **Figure 3. ocEAn, a tool to visualize metabolic changes in cancer cells. A)** Representative
984 scatter plot generated using ocEAn for BCAT1 in the indicated comparisons. Metabolites
985 upstream and downstream of BCAT1 directly or indirectly linked to reaction are indicated in
986 two separate plots, one (on top) for conversion of leucine in ketoisocaproic acid (KIC), the other
987 (on the bottom) for the transamination of α -ketoglutarate (aKG) to glutamate. The dot size
988 represents the multiplication of the t-value with the weighted distance index (distance index
989 being the number of the x-axis). y-axis reports the t-value of the abundances for the metabolites
990 indicated in BCAT1 footprint including if they are accumulated or depleted upstream or
991 downstream. The most relevant metabolites are highlighted in green. **B)** Proportion of total
992 pool of the indicated labelled metabolites originating from ^{13}C leucine+isoleucine (top) in all
993 renal cells at the indicated time points. Values are normalized to total ion count. Data represent
994 the mean of 5 independent cultures \pm SD. p-values were calculated using one-way ANOVA
995 with multiple comparisons.

996

997 **Figure 4. BCAT transamination supplies nitrogen for aspartate and nucleotide**
998 **biosynthesis in ccRCC. A)** Diagram of the labelling pattern originating from ^{15}N leucine
999 catabolism. The grey circles indicate unlabeled N, blue circle ^{15}N , white circles represent
1000 unlabeled carbons. Measured metabolites through LC-MS are indicated in blue circles.
1001 BCAT1/2= Branched Chain Amino Acid Transaminase 1/2; GOT1/2= Glutamic-Oxaloacetic
1002 Transaminase 1/2. ASNS= Asparagine Synthase; ASS1= Argininosuccinate Synthase; ASL=
1003 Argininosuccinate Lyase. Abundance of labelled leucine m+1 and glutamate m+1 (**B**),
1004 aspartate m+1 and asparagine m+1 (**C**) originating from ^{15}N leucine after 27h normalized to
1005 total ion count. Data represent the mean of 6 independent cultures \pm SD. p-values were
1006 calculated using one-way ANOVA with multiple comparisons. **D)** Proportion of total pool of
1007 the indicated labelled metabolites originating from ^{15}N leucine after 24h in culture with
1008 EBSS+FBS 2.5% acids for 24h. Data are normalized to total ion count and represent the mean
1009 of 6 independent cultures \pm SD. p-values were calculated using one-way ANOVA with multiple
1010 comparisons. **E-G)** Intracellular abundance of the indicated metabolites after treatment with
1011 BCAT1 100 μM in Plasmax for 22h. Values are normalized to total ion count and expressed as
1012 the mean of 6 independent cultures \pm SD. p-values were calculated using one-way ANOVA
1013 with multiple comparisons.

1014

1015 **Figure 5. VHL reconstitution restored BCAA functioning in ccRCC cells. A)** Heatmap
1016 showing the enriched pathways in the indicated comparisons obtained through GSEA analysis
1017 of proteomics data generated from cells grown in RPMI. **B)** Volcano plot showing the
1018 differential expression of genes that belong to KEGG 'Valine leucine and isoleucine
1019 degradation' signature in 786-O+VHL vs 786-O+EV and 786-M1A+VHL vs 786-M1A+EV
1020 from proteomics data obtained culturing cells in RPMI. FC= fold change; red=upregulated
1021 genes, blue=downregulated genes. **C)** Ratio of the intracellular abundance of C3-carnitines and
1022 C5-carnitines in RPMI in cells expressing VHL compared to EV. Data were normalized to total
1023 ion count and represent the mean of 3 independent experiments (N=3) \pm S.E.M. p-values were
1024 calculated using paired t-test on log(ratio). **D)** Proportion of total pool of the indicated labelled
1025 metabolites originating from ^{13}C leucine (top) and relative abundance of labelled KIC+KMV,
1026 C5-carnitine, C3-carnitine. Cells were grown for 24h in RPMI+ ^{13}C leucine. Data represent the
1027 mean of 5 independent cultures \pm SD. p-values were calculated using one-way ANOVA with

1028 multiple comparisons. **E)** mRNA levels of *SLC7A5* in the indicated cell lines grown in RPMI
1029 measured through qPCR. *TBP* was used as endogenous control. Values represent relative
1030 quantification (RQ) \pm error calculated using Expression suite software (Applied biosystem)
1031 calculated using SD algorithm. p-value was calculated through Expression suite software. N=3
1032 independent experiments.

1033

1034 **Fig.6 ASS1 re-expression in metastatic ccRCC confers resistance to arginine depletion**

1035 **and supports metastatic invasion *in vitro* and *in vivo*.** **A)** Proportion of the total pool of the

1036 indicated labelled metabolites originating from ¹⁵N leucine (top) and abundance of labelled

1037 leucine m+1, glutamate m+1, aspartate m+1 (bottom) after 27h normalized to total ion count.

1038 Data represent the mean of 6 independent cultures \pm SD. p-values were calculated using one-

1039 way ANOVA with multiple comparisons. **B)** Volcano of the differentially regulated metabolic

1040 genes comparing 786-M1A vs 786-O using RNA-seq data generated from cells grown in

1041 Plasmax. red= indicates upregulated genes, blue=downregulated genes. FC=fold change. **C)**

1042 Argininosuccinate abundance in the indicated cell lines cultured in Plasmax measured using

1043 LC-MS. Data were normalized to total ion count and represent the mean of 3 independent

1044 experiments (N=3) \pm S.E.M. p-values were calculated using one-way ANOVA with multiple

1045 comparisons. **D)** Heatmap of the methylation level (B-value) of the indicated CGs within a

1046 CpG island overlapping with *ASS1* TSS. Values are presented as the mean of two independent

1047 experiments (N=2). **E)** mRNA levels of *ASS1* in 786-O treated for 72h with either vehicle or

1048 200nM 5AC measured through qPCR. *TBP* was used as endogenous control. Values represent

1049 relative quantification (RQ) \pm error calculated using Expression suite software (Applied

1050 biosystem) calculated using SD algorithm. p-value was calculated through Expression suite

1051 software. N=3 independent experiments. **F)** Measurement of cell proliferation through

1052 Sulforhodamine B (SRB) staining after treatment with pegylated arginine deiminase

1053 (ADIPEG20, 57.5 ng/ml) at the indicated concentrations for 48h. Values of SRB absorbance

1054 are shown as fold change \pm S.E.M. relative to vehicle-treated staining. p-values were calculated

1055 using one-way ANOVA with multiple comparisons. N=4 independent experiments. **G)** mRNA

1056 levels of *ASS1* and *CXCR4* in 786-O treated with ADIPEG20 57.5 ng/ml for 4 weeks, measured

1057 through qPCR. *TBP* was used as endogenous control. Values represent relative quantification

1058 (RQ) \pm error calculated using Expression suite software (Applied biosystem) calculated using

1059 SD algorithm. p-value was calculated through Expression suite software from N=3 independent

1060 experiments. **H)** Western blot of the *ASS1* levels in cells stably cultured in Plasmax upon *ASS1*

1061 silencing using two different shRNA constructs. Calnexin was used as an endogenous control.

1062 **I)** Measurement of 786-M1A cell proliferation after silencing of *ASS1* using Incucyte.

1063 Confluency values are shown as phase image sharpness calculated through Incucyte software

1064 \pm S.E.M. N=3 independent experiments. **J)** Representative images of the indicated cell lines at

1065 time 0 and after 48h (left) upon growth as spheroids in collagen (area marked in red). Pictures

1066 were obtained from Incucyte. Scale bar is 500 μ m (Right) Quantification of the cell spreading

1067 in the collagen matrix at time 48h. N=3 independent experiments. Statistical significance was

1068 calculated using unpaired t-test. **K)** Normalized lung photon flux from the lungs of 5 mice post

1069 tail-vein inoculation of 300,000 cells for the indicated cell types. **L)** Box plot of the normalized

1070 lung photon flux at day 38 post-inoculation (left) from the experiment shown in L and

1071 representative bioluminescence images of the mice at day 38 (**M**). Statistical significance was

1072 calculated using one-way ANOVA with multiple comparisons. **N)** Representative images of

1073 human vimentin/hematoxylin immunohistochemistry of mouse lungs sections after inoculation

1074 of cells in the tail vein for the indicated cell types. Scale bar is 200 μ m.

1075

1076 **Figure 7. Reprogramming of the BCAA amino acid catabolism is intertwined with the**

1077 **urea cycle enzymes during ccRCC progression.** Schematic showing a summary of the

1078 metabolic reprogramming in renal cancer cells during progression. Upon *VHL* loss, renal
1079 cancer cells activate a metabolic reprogramming to compensate for the aspartate defect that is
1080 a consequence of the HIF-dependent mitochondrial dysfunction present in these cells that
1081 involves combined activation of *BCAT1* and *GOT1*. HIFs activation suppresses *ASS1*, sparing
1082 aspartate from consumption through urea cycle and favoring its re-direction towards nucleotide
1083 biosynthesis. In the metastatic population, *ASS1* is epigenetically re-activated, and its
1084 expression is triggered also by low levels of arginine in the microenvironment. *ASS1*
1085 reactivation in the metastatic cells connects the BCAA catabolism reprogramming to the urea
1086 cycle, providing metastatic cells with the capability to derive arginine from BCAA and to
1087 survive in the presence of rate limiting levels of arginine.
1088

1089 **Supplementary Figure 1-related to Figure 1. Expression of the BCAA degradation**
1090 **pathway and TCGA patients' survival.** **A)** Bar plot showing the significance of the
1091 correlation between BCAA catabolism expression and patients' survival expressed as $\log_{10}(\text{p-value})$ for all TCGA tumors. **B)** Overall survival of KIRP and COAD patients obtained through
1092 GEPIA, based on gene expression of KEGG 'valine, leucine and isoleucine degradation'
1093 signature. Cut-off used for high/low groups was 50% and p-value displayed as $-\log_{\text{rank}}(\text{p-value})$. Dotted line refers to the survival with a confidence interval (CI) of 95%. n=number of
1094 samples compared; HR=hazard ratio based on the Cox PH model. KIRP= renal papillary
1095 carcinoma, COAD= colorectal tumors.
1096
1097
1098

1099 **Supplementary Figure 2-related to Figure 2. ccRCC cells cultured in Plasmax resemble**
1100 **the metabolic and transcriptional profile of renal tumors.** **A)** Heatmap showing the
1101 correlation score between the metabolic profile of cells cultured in RPMI or Plasmax vs renal
1102 tumors (TU) and healthy tissues, (KI) from Dugourd et al. 2021. **B)** Dot plot of the
1103 Transcription factor (TF) score performed on RNA-seq data from cells cultured in Plasmax
1104 comparing 786-O vs HK2 (green), 786-M1A vs HK2 (orange) ranked by significance. The
1105 dimension of the dots is based on the $-\log_{10}(\text{adj-p-value})$. NES= normalized enrichment score.
1106 **C)** Bar plot showing the normalized count of the mRNA for the indicated genes from RNA-
1107 seq generated upon cells grown in Plasmax. Significance was calculated using unpaired t-test
1108 on \log_2 -transformed counts. RNA-seq dataset was generated from 3 independent cultures. **D)**
1109 Volcano plot showing the differential expression of proteins that belong to KEGG 'Valine
1110 leucine and isoleucine degradation' signature in 786-O compared to renal normal cells HK2.
1111 FC=fold change; red=upregulated genes, blue=downregulated genes. **E)** Cellular respiration of
1112 the indicated cell line cultured in Plasmax using Sea Horse Extracellular flux analyzer XF24.
1113 OCR=oxygen consumption rate normalized for protein content/well. Values are represented as
1114 the mean of 4 independent cultures \pm SD. **F)** Abundance of the indicated metabolites from
1115 BCAA catabolism in the indicated cell lines measured using LC-MS. Data were normalized to
1116 total ion count and represent the mean of 3 independent experiments (N=3) \pm S.E.M. p-values
1117 were calculated using one-way ANOVA with multiple comparisons. **G)** Consumption/release
1118 of the indicated metabolites from the medium normalized to dry weight generation at t=24
1119 (dW). Significance was calculated using one-way ANOVA with multiple comparisons. **H)**
1120 Expression of the indicated proteins measured through labelled-free quantification (LFQ) from
1121 the proteomic dataset in the indicated cell lines. Significance was calculated using one-way
1122 ANOVA with multiple comparisons. SLC7A5=Solute Carrier Family 7 Member 5;
1123 SLC3A2=Solute Carrier Family 3 Member 2
1124

1125 **Supplementary Figure 3-related to Figure 3. BCAA catabolism does not provide carbons**
1126 **for the TCA cycle in ccRCC.** **A)** Schematics showing how ocEAn computes the footprint for

1127 metabolic enzymes. **B)** Diagram of the labelling pattern originating from ^{13}C
1128 leucine+isoleucine catabolism. The green circles indicate ^{13}C , white circles represent unlabeled
1129 carbons. Measured metabolites through LC-MS are indicated in green circles. BCAT1/2=
1130 Branched Chain Amino Acid Transaminase 1/2; BCKDH = Branched Chain Keto Acid
1131 Dehydrogenase complex; KIC= ketoisocaproate. KMV=ketomethylvalerate. **C)** Proportion of
1132 total pool of the indicated labelled metabolites originating from ^{13}C leucine+isoleucine after
1133 43h in the indicated cell lines. Data represent the mean of 5 independent cultures \pm SD. p-values
1134 were calculated using one-way ANOVA with multiple comparisons.

1135

1136 **Supplementary Figure 4-related to Figure 4. BCAT transamination supplies nitrogen for**
1137 **aspartate biosynthesis in different ccRCC cell lines.** **A)** Heatmap showing the relative
1138 percentage of labelled metabolites m+1 on the nitrogen derived from ^{15}N Leucine, from the
1139 experiment indicated in Figure 4A. **B)** Labelled-free quantification (LFQ) of the indicated
1140 proteins based on proteomics dataset generated after culturing cells in Plasmax. Significance
1141 was calculated using one-way ANOVA with multiple comparisons. **C)** Abundances of labelled
1142 leucine m+1, glutamate m+1, aspartate m+1 and asparagine m+1 originating from ^{15}N
1143 leucine+isoleucine in Plasmax after 27h in additional ccRCC cells lines. Data are normalized
1144 to total ion count and represent the mean of 6 independent cultures \pm SD. p-values were
1145 calculated using one-way ANOVA with multiple comparisons. **D)** Proportion of total pool of
1146 intracellular leucine after incubation of the cells with ^{15}N leucine EBSS+FBS 2.5% for 24h.
1147 Data represent the mean of 6 independent cultures \pm SD. p-values were calculated using one-
1148 way ANOVA with multiple comparisons. **E)** Intracellular abundance of the indicated
1149 metabolites after treatment with BCATI 100 μM in Plasmax for 22h. Values are normalized to
1150 total ion count and expressed as the mean of 6 independent cultures \pm SD. p-values were
1151 calculated using one-way ANOVA with multiple comparisons.

1152

1153 **Supplementary Figure 5-related to Figure 5. VHL reconstitution restores mitochondrial**
1154 **function and aspartate level in ccRCC cells.** **A)** mRNA levels of *VHL* in the indicated cell
1155 lines grown in RPMI through qPCR. *TBP* was used as endogenous control. Values represent
1156 relative quantification (RQ) \pm error calculated using Expression suite software (Applied
1157 biosystem) calculated using SD algorithm. p-values were calculated through Expression suite
1158 software. N=3 independent experiments. **B)** Cellular respiration of the indicated cell line
1159 cultured in RPMI after VHL re-expression using Sea Horse Extracellular flux analyzer XF24.
1160 OCR=oxygen consumption rate normalized for protein content/well. Values are represented as
1161 the mean of 3 independent experiments \pm S.E.M. (N=3). **C)** Ratio of the intracellular abundance
1162 of aspartate in cells grown in RPMI expressing VHL compared to EV. Data were normalized
1163 to total ion count and represent the mean of 8 independent experiments (N=8) \pm S.E.M. p-values
1164 were calculated using paired t-test on log(ratio). **D)** Proportion of total pool of the intracellular
1165 leucine. Cells were grown for 24h in RPMI+ ^{13}C leucine. Data represent the mean of 5
1166 independent cultures \pm SD. p-values were calculated using one-way ANOVA with multiple
1167 comparisons.

1168

1169 **Supplementary Figure 6-related to Figure 6. ASS1 expression in metastatic OS-LM1 cells**
1170 **and advanced ccRCC tumors.** **A)** Schematics of the urea shunt in renal cells (left) and
1171 Arginase 2 (ARG2), argininosuccinate synthase (ASS1) and argininosuccinate lyase (ASL)
1172 protein expression (right) measured through labelled-free quantification (LFQ) from the
1173 proteomic dataset in the indicated cell lines. Significance was calculated using one-way
1174 ANOVA with multiple comparisons. **B)** Western blot of the ASS1 levels in cells stably cultured
1175 in Plasmax. Calnexin was used as an endogenous control. **C)** Consumption/release of arginine,
1176 ornithine and citrulline from medium normalized to dry weight generation at t=24 (dW) in the

1177 indicated cells lines. Data represent the mean of 5 independent cultures \pm SD. p-values were
1178 calculated using one-way ANOVA with multiple comparisons. **D)** Graphical visualization of
1179 the acetylation H3k27ac peaks for the genomic region around ASS1 gene in 786-O and 786-
1180 M1A generated using IGV software. Data were previously generated (Rodrigues et al.2018)
1181 from cells grown in RPMI. **E)** mRNA levels of ASS1 in OS-RC-2 and OS-LM1 through qPCR.
1182 *TBP* was used as endogenous control. Values represent relative quantification (RQ) \pm error
1183 calculated using Expression suite software (Applied biosystem) calculated using SD algorithm.
1184 p-values were calculated through Expression suite software. N=4 independent experiments. **F)**
1185 Western blot of ASS1 protein level in cells indicated stably cultured in Plasmax. Calnexin was
1186 used as an endogenous control. **G)** Heatmap showing the methylation level (B-value) of the
1187 indicated CG from a CpG island overlapping with ASS1 TSS. values are presented as the mean
1188 of two independent experiments in OS-RC-2 and OS-LM1 cells of cells grown in RPMI. **H)**
1189 mRNA levels of ASS1 in OS-RC-2 and OS-LM1 treated for 72h with either vehicle or 5AC
1190 200nM measured through qPCR. *TBP* was used as endogenous control. Values represent
1191 relative quantification (RQ) \pm error calculated using Expression suite software (Applied
1192 biosystem) calculated using SD algorithm. p-values were calculated through Expression suite
1193 software. N=3 independent experiments. **I)** Volcano plot of the metabolic genes differentially
1194 expressed in a cluster of TCGA KIRC advanced tumors (Stage III+IV) where ASS1 expression
1195 is high (*ASS1^{high}*) or low (*ASS1^{low}*) compared to tumors from Stage I+II. Fold change is
1196 expressed as log₂FC. Y axis represents -log₁₀(p-value). **J)** GSEA of the pathways expressed
1197 in a cluster of TCGA KIRC advanced tumors (Stage III+IV) where ASS1 expression is higher
1198 (*ASS1^{high}*) or lower (*ASS1^{low}*) compared to tumors from Stage I+II. NES=normalized
1199 enrichment score. **K)** Ratio of the argininosuccinate measured through LC-MS in cohort of
1200 ccRCC patients' primary tumors that were metastatic at the time normalized to healthy matched
1201 tissue. **L)** Arginine levels in the tissue or the interstitial fluid from mouse renal and lung tissues.
1202 Data represent the mean of 8 mice \pm S.E.M. p-values were calculated using one-way ANOVA
1203 with multiple comparisons.
1204

1205 **References**

1206 Alkan, H.F., and Bogner-Strauss, J.G. (2019). Maintaining cytosolic aspartate levels is a major
1207 function of the TCA cycle in proliferating cells. *Mol Cell Oncol* 6, e1536843.
1208 Allen, M.D., Luong, P., Hudson, C., Leyton, J., Delage, B., Ghazaly, E., Cutts, R., Yuan, M., Syed, N., Lo
1209 Nigro, C., et al. (2014). Prognostic and therapeutic impact of argininosuccinate synthetase 1 control
1210 in bladder cancer as monitored longitudinally by PET imaging. *Cancer Res* 74, 896-907.
1211 Aurich, M.K., and Thiele, I. (2016). Computational Modeling of Human Metabolism and Its
1212 Application to Systems Biomedicine. *Methods Mol Biol* 1386, 253-281.
1213 Berg, J.A., Zhou, Y., Waller, T.C., Ouyang, Y., Nowinski, S.M., Van Ry, T., George, I., Cox, J.E., Wang, B.,
1214 and Rutter, J. (2020). Gazing into the Metaverse: Automated exploration and contextualization of
1215 metabolic data. *bioRxiv*, 2020.2006.2025.171850.
1216 Bergers, G., and Fendt, S.M. (2021). The metabolism of cancer cells during metastasis. *Nat Rev*
1217 *Cancer* 21, 162-180.
1218 Birsoy, K., Wang, T., Chen, W.W., Freinkman, E., Abu-Remaileh, M., and Sabatini, D.M. (2015). An
1219 Essential Role of the Mitochondrial Electron Transport Chain in Cell Proliferation Is to Enable
1220 Aspartate Synthesis. *Cell* 162, 540-551.
1221 Bleu, M., Gaulis, S., Lopes, R., Sprouffske, K., Apfel, V., Holwerda, S., Pregnolato, M., Yildiz, U., Cordo,
1222 V., Dost, A.F.M., et al. (2019). PAX8 activates metabolic genes via enhancer elements in Renal Cell
1223 Carcinoma. *Nat Commun* 10, 3739.

- 1224 Cantor, J.R., Abu-Remaileh, M., Kanarek, N., Freinkman, E., Gao, X., Louissaint, A., Jr., Lewis, C.A., and
1225 Sabatini, D.M. (2017). Physiologic Medium Rewires Cellular Metabolism and Reveals Uric Acid as an
1226 Endogenous Inhibitor of UMP Synthase. *Cell* *169*, 258-272 e217.
- 1227 Choueiri, T.K., and Motzer, R.J. (2017). Systemic Therapy for Metastatic Renal-Cell Carcinoma. *N Engl*
1228 *J Med* *376*, 354-366.
- 1229 Clark, D.J., Dhanasekaran, S.M., Petralia, F., Pan, J., Song, X., Hu, Y., da Veiga Leprevost, F., Reva, B.,
1230 Lih, T.M., Chang, H.Y., et al. (2019). Integrated Proteogenomic Characterization of Clear Cell Renal
1231 Cell Carcinoma. *Cell* *179*, 964-983 e931.
- 1232 Creighton, C.J., Morgan, M., Gunaratne, P.H., Wheeler, D.A., Gibbs, R.A., Gordon Robertson, A., Chu,
1233 A., Beroukhi, R., Cibulskis, K., Signoretti, S., et al. (2013). Comprehensive molecular
1234 characterization of clear cell renal cell carcinoma. *Nature* *499*, 43-49.
- 1235 Dugourd, A., Kuppe, C., Sciacovelli, M., Gjerga, E., Gabor, A., Emdal, K.B., Vieira, V., Bekker-Jensen,
1236 D.B., Kranz, J., Bindels, E.M.J., et al. (2021). Causal integration of multi-omics data with prior
1237 knowledge to generate mechanistic hypotheses. *Mol Syst Biol* *17*, e9730.
- 1238 Elia, I., Doglioni, G., and Fendt, S.M. (2018). Metabolic Hallmarks of Metastasis Formation. *Trends*
1239 *Cell Biol* *28*, 673-684.
- 1240 Elorza, A., Soro-Arnaiz, I., Melendez-Rodriguez, F., Rodriguez-Vaello, V., Marsboom, G., de Carcer, G.,
1241 Acosta-Iborra, B., Albacete-Albacete, L., Ordonez, A., Serrano-Oviedo, L., et al. (2012). HIF2alpha acts
1242 as an mTORC1 activator through the amino acid carrier SLC7A5. *Mol Cell* *48*, 681-691.
- 1243 Fendt, S.M., Frezza, C., and Erez, A. (2020). Targeting Metabolic Plasticity and Flexibility Dynamics for
1244 Cancer Therapy. *Cancer Discov* *10*, 1797-1807.
- 1245 Garcia-Bermudez, J., Baudrier, L., La, K., Zhu, X.G., Fidelin, J., Sviderskiy, V.O., Papagiannakopoulos,
1246 T., Molina, H., Snuderl, M., Lewis, C.A., et al. (2018). Aspartate is a limiting metabolite for cancer cell
1247 proliferation under hypoxia and in tumours. *Nat Cell Biol* *20*, 775-781.
- 1248 Gatto, F., Nookaew, I., and Nielsen, J. (2014). Chromosome 3p loss of heterozygosity is associated
1249 with a unique metabolic network in clear cell renal carcinoma. *Proc Natl Acad Sci U S A* *111*, E866-
1250 875.
- 1251 Gaude, E., and Frezza, C. (2016). Tissue-specific and convergent metabolic transformation of cancer
1252 correlates with metastatic potential and patient survival. *Nat Commun* *7*, 13041.
- 1253 Gaude, E., Schmidt, C., Gammage, P.A., Dugourd, A., Blacker, T., Chew, S.P., Saez-Rodriguez, J.,
1254 O'Neill, J.S., Szabadkai, G., Minczuk, M., et al. (2018). NADH Shuttling Couples Cytosolic Reductive
1255 Carboxylation of Glutamine with Glycolysis in Cells with Mitochondrial Dysfunction. *Mol Cell* *69*, 581-
1256 593 e587.
- 1257 Goncalves, E., Sciacovelli, M., Costa, A.S.H., Tran, M.G.B., Johnson, T.I., Machado, D., Frezza, C., and
1258 Saez-Rodriguez, J. (2018). Post-translational regulation of metabolism in fumarate hydratase
1259 deficient cancer cells. *Metab Eng* *45*, 149-157.
- 1260 Hakimi, A.A., Reznik, E., Lee, C.H., Creighton, C.J., Brannon, A.R., Luna, A., Aksoy, B.A., Liu, E.M.,
1261 Shen, R., Lee, W., et al. (2016). An Integrated Metabolic Atlas of Clear Cell Renal Cell Carcinoma.
1262 *Cancer Cell* *29*, 104-116.
- 1263 Hanahan, D., and Weinberg, R.A. (2011). Hallmarks of cancer: the next generation. *Cell* *144*, 646-674.
- 1264 Huang, H.Y., Wu, W.R., Wang, Y.H., Wang, J.W., Fang, F.M., Tsai, J.W., Li, S.H., Hung, H.C., Yu, S.C.,
1265 Lan, J., et al. (2013). ASS1 as a novel tumor suppressor gene in myxofibrosarcomas: aberrant loss via
1266 epigenetic DNA methylation confers aggressive phenotypes, negative prognostic impact, and
1267 therapeutic relevance. *Clin Cancer Res* *19*, 2861-2872.
- 1268 Keshet, R., Szlosarek, P., Carracedo, A., and Erez, A. (2018). Rewiring urea cycle metabolism in cancer
1269 to support anabolism. *Nat Rev Cancer* *18*, 634-645.
- 1270 Kremer, J.C., Prudner, B.C., Lange, S.E.S., Bean, G.R., Schultze, M.B., Brashears, C.B., Radyk, M.D.,
1271 Redlich, N., Tzeng, S.C., Kami, K., et al. (2017). Arginine Deprivation Inhibits the Warburg Effect and
1272 Upregulates Glutamine Anaplerosis and Serine Biosynthesis in ASS1-Deficient Cancers. *Cell Rep* *18*,
1273 991-1004.

- 1274 Kreuzaler, P., Panina, Y., Segal, J., and Yuneva, M. (2020). Adapt and conquer: Metabolic flexibility in
1275 cancer growth, invasion and evasion. *Mol Metab* 33, 83-101.
- 1276 LaGory, E.L., Wu, C., Taniguchi, C.M., Ding, C.C., Chi, J.T., von Eyben, R., Scott, D.A., Richardson, A.D.,
1277 and Giaccia, A.J. (2015). Suppression of PGC-1 α Is Critical for Reprogramming Oxidative
1278 Metabolism in Renal Cell Carcinoma. *Cell Rep* 12, 116-127.
- 1279 Lan, J., Tai, H.C., Lee, S.W., Chen, T.J., Huang, H.Y., and Li, C.F. (2014). Deficiency in expression and
1280 epigenetic DNA Methylation of ASS1 gene in nasopharyngeal carcinoma: negative prognostic impact
1281 and therapeutic relevance. *Tumour Biol* 35, 161-169.
- 1282 Li, B., Qiu, B., Lee, D.S., Walton, Z.E., Ochocki, J.D., Mathew, L.K., Mancuso, A., Gade, T.P., Keith, B.,
1283 Nissim, I., et al. (2014). Fructose-1,6-bisphosphatase opposes renal carcinoma progression. *Nature*
1284 513, 251-255.
- 1285 Mayers, J.R., Torrence, M.E., Danai, L.V., Papagiannakopoulos, T., Davidson, S.M., Bauer, M.R., Lau,
1286 A.N., Ji, B.W., Dixit, P.D., Hosios, A.M., et al. (2016). Tissue of origin dictates branched-chain amino
1287 acid metabolism in mutant Kras-driven cancers. *Science* 353, 1161-1165.
- 1288 McAlpine, J.A., Lu, H.T., Wu, K.C., Knowles, S.K., and Thomson, J.A. (2014). Down-regulation of
1289 argininosuccinate synthetase is associated with cisplatin resistance in hepatocellular carcinoma cell
1290 lines: implications for PEGylated arginine deiminase combination therapy. *BMC Cancer* 14, 621.
- 1291 McBrayer, S.K., Mayers, J.R., DiNatale, G.J., Shi, D.D., Khanal, J., Chakraborty, A.A., Sarosiek, K.A.,
1292 Briggs, K.J., Robbins, A.K., Sewastianik, T., et al. (2018). Transaminase Inhibition by 2-
1293 Hydroxyglutarate Impairs Glutamate Biosynthesis and Redox Homeostasis in Glioma. *Cell* 175, 101-
1294 116 e125.
- 1295 Mullen, A.R., Wheaton, W.W., Jin, E.S., Chen, P.H., Sullivan, L.B., Cheng, T., Yang, Y., Linehan, W.M.,
1296 Chandel, N.S., and DeBerardinis, R.J. (2011). Reductive carboxylation supports growth in tumour cells
1297 with defective mitochondria. *Nature* 481, 385-388.
- 1298 Nam, H., Kundu, A., Karki, S., Brinkley, G., Chandrashekar, D.S., Kirkman, R.L., Liu, J., Liberti, M.V.,
1299 Locasale, J.W., Mitchell, T., et al. (2021). TGF- β signaling suppresses TCA cycle metabolism in renal
1300 cancer. *bioRxiv*, 2021.2002.2019.429599.
- 1301 Neinast, M., Murashige, D., and Arany, Z. (2019a). Branched Chain Amino Acids. *Annu Rev Physiol*
1302 81, 139-164.
- 1303 Neinast, M.D., Jang, C., Hui, S., Murashige, D.S., Chu, Q., Morscher, R.J., Li, X., Zhan, L., White, E.,
1304 Anthony, T.G., et al. (2019b). Quantitative Analysis of the Whole-Body Metabolic Fate of Branched-
1305 Chain Amino Acids. *Cell Metab* 29, 417-429 e414.
- 1306 Nicholson, L.J., Smith, P.R., Hiller, L., Szlosarek, P.W., Kimberley, C., Sehouli, J., Koensgen, D., Mustea,
1307 A., Schmid, P., and Crook, T. (2009). Epigenetic silencing of argininosuccinate synthetase confers
1308 resistance to platinum-induced cell death but collateral sensitivity to arginine auxotrophy in ovarian
1309 cancer. *Int J Cancer* 125, 1454-1463.
- 1310 Ochocki, J.D., Khare, S., Hess, M., Ackerman, D., Qiu, B., Daisak, J.I., Worth, A.J., Lin, N., Lee, P., Xie,
1311 H., et al. (2018). Arginase 2 Suppresses Renal Carcinoma Progression via Biosynthetic Cofactor
1312 Pyridoxal Phosphate Depletion and Increased Polyamine Toxicity. *Cell Metab* 27, 1263-1280 e1266.
- 1313 Onishi, Y., Hiraiwa, M., Kamada, H., Iezaki, T., Yamada, T., Kaneda, K., and Hinoi, E. (2019). Hypoxia
1314 affects Slc7a5 expression through HIF-2 α in differentiated neuronal cells. *FEBS Open Bio* 9, 241-
1315 247.
- 1316 Pandey, N., Lanke, V., and Vinod, P.K. (2020). Network-based metabolic characterization of renal cell
1317 carcinoma. *Sci Rep* 10, 5955.
- 1318 Pascual, G., Dominguez, D., and Benitah, S.A. (2018). The contributions of cancer cell metabolism to
1319 metastasis. *Dis Model Mech* 11.
- 1320 Pavlova, N.N., and Thompson, C.B. (2016). The Emerging Hallmarks of Cancer Metabolism. *Cell*
1321 *Metab* 23, 27-47.
- 1322 Rabinovich, S., Adler, L., Yizhak, K., Sarver, A., Silberman, A., Agron, S., Stettner, N., Sun, Q., Brandis,
1323 A., Helbling, D., et al. (2015). Diversion of aspartate in ASS1-deficient tumours fosters de novo
1324 pyrimidine synthesis. *Nature* 527, 379-383.

1325 Raffel, S., Falcone, M., Kneisel, N., Hansson, J., Wang, W., Lutz, C., Bullinger, L., Poschet, G.,
1326 Nonnenmacher, Y., Barnert, A., et al. (2017). BCAT1 restricts alphaKG levels in AML stem cells
1327 leading to IDHmut-like DNA hypermethylation. *Nature* 551, 384-388.
1328 Ricketts, C.J., De Cubas, A.A., Fan, H., Smith, C.C., Lang, M., Reznik, E., Bowlby, R., Gibb, E.A., Akbani,
1329 R., Beroukhi, R., et al. (2018). The Cancer Genome Atlas Comprehensive Molecular
1330 Characterization of Renal Cell Carcinoma. *Cell Rep* 23, 3698.
1331 Rodrigues, P., Patel, S.A., Harewood, L., Olan, I., Vojtasova, E., Syafruddin, S.E., Zaini, M.N.,
1332 Richardson, E.K., Burge, J., Warren, A.Y., et al. (2018). NF-kappaB-Dependent Lymphoid Enhancer Co-
1333 option Promotes Renal Carcinoma Metastasis. *Cancer Discov* 8, 850-865.
1334 Ryan, D.G., Yang, M., Prag, H.A., Blanco, G.R., Nikitopoulou, E., Segarra-Mondejar, M., Powell, C.A.,
1335 Young, T., Burger, N., Miljkovic, J.L., et al. (2021). Disruption of the TCA cycle reveals an ATF4-
1336 dependent integration of redox and amino acid metabolism. *bioRxiv*, 2021.2007.2027.453996.
1337 Sciacovelli, M., Goncalves, E., Johnson, T.I., Zecchini, V.R., da Costa, A.S., Gaude, E., Drubbel, A.V.,
1338 Theobald, S.J., Abbo, S.R., Tran, M.G., et al. (2016). Fumarate is an epigenetic modifier that elicits
1339 epithelial-to-mesenchymal transition. *Nature* 537, 544-547.
1340 Sivanand, S., and Vander Heiden, M.G. (2020). Emerging Roles for Branched-Chain Amino Acid
1341 Metabolism in Cancer. *Cancer Cell* 37, 147-156.
1342 Sullivan, L.B., Gui, D.Y., Hosios, A.M., Bush, L.N., Freinkman, E., and Vander Heiden, M.G. (2015).
1343 Supporting Aspartate Biosynthesis Is an Essential Function of Respiration in Proliferating Cells. *Cell*
1344 162, 552-563.
1345 Syed, N., Langer, J., Janczar, K., Singh, P., Lo Nigro, C., Lattanzio, L., Coley, H.M., Hatzimichael, E.,
1346 Bomalaski, J., Szlosarek, P., et al. (2013). Epigenetic status of argininosuccinate synthetase and
1347 argininosuccinate lyase modulates autophagy and cell death in glioblastoma. *Cell Death Dis* 4, e458.
1348 Torrano, V., Valcarcel-Jimenez, L., Cortazar, A.R., Liu, X., Urosevic, J., Castillo-Martin, M., Fernandez-
1349 Ruiz, S., Morciano, G., Caro-Maldonado, A., Guiu, M., et al. (2016). The metabolic co-regulator
1350 PGC1alpha suppresses prostate cancer metastasis. *Nat Cell Biol* 18, 645-656.
1351 Valcarcel-Jimenez, L., Macchia, A., Crosas-Molist, E., Schaub-Clerigue, A., Camacho, L., Martin-
1352 Martin, N., Cicogna, P., Viera-Bardon, C., Fernandez-Ruiz, S., Rodriguez-Hernandez, I., et al. (2019).
1353 PGC1alpha Suppresses Prostate Cancer Cell Invasion through ERRalpha Transcriptional Control.
1354 *Cancer Res* 79, 6153-6165.
1355 Vande Voorde, J., Ackermann, T., Pfetzer, N., Sumpton, D., Mackay, G., Kalna, G., Nixon, C., Blyth, K.,
1356 Gottlieb, E., and Tardito, S. (2019). Improving the metabolic fidelity of cancer models with a
1357 physiological cell culture medium. *Sci Adv* 5, eaau7314.
1358 Vander Heiden, M.G., and DeBerardinis, R.J. (2017). Understanding the Intersections between
1359 Metabolism and Cancer Biology. *Cell* 168, 657-669.
1360 Vanharanta, S., Shu, W., Brenet, F., Hakimi, A.A., Heguy, A., Viale, A., Reuter, V.E., Hsieh, J.J.,
1361 Scandura, J.M., and Massague, J. (2013). Epigenetic expansion of VHL-HIF signal output drives
1362 multiorgan metastasis in renal cancer. *Nat Med* 19, 50-56.
1363 Wallace, M., Green, C.R., Roberts, L.S., Lee, Y.M., McCarville, J.L., Sanchez-Gurmaches, J., Meurs, N.,
1364 Gengatharan, J.M., Hover, J.D., Phillips, S.A., et al. (2018). Enzyme promiscuity drives branched-chain
1365 fatty acid synthesis in adipose tissues. *Nat Chem Biol* 14, 1021-1031.
1366 Wettersten, H.I., Aboud, O.A., Lara, P.N., Jr., and Weiss, R.H. (2017). Metabolic reprogramming in
1367 clear cell renal cell carcinoma. *Nat Rev Nephrol* 13, 410-419.
1368 Young, M.D., Mitchell, T.J., Vieira Braga, F.A., Tran, M.G.B., Stewart, B.J., Ferdinand, J.R., Collord, G.,
1369 Botting, R.A., Popescu, D.M., Loudon, K.W., et al. (2018). Single-cell transcriptomes from human
1370 kidneys reveal the cellular identity of renal tumors. *Science* 361, 594-599.
1371 Zhang, B., Chen, Y., Shi, X., Zhou, M., Bao, L., Hatanpaa, K.J., Patel, T., DeBerardinis, R.J., Wang, Y.,
1372 and Luo, W. (2021). Regulation of branched-chain amino acid metabolism by hypoxia-inducible
1373 factor in glioblastoma. *Cell Mol Life Sci* 78, 195-206.

1374

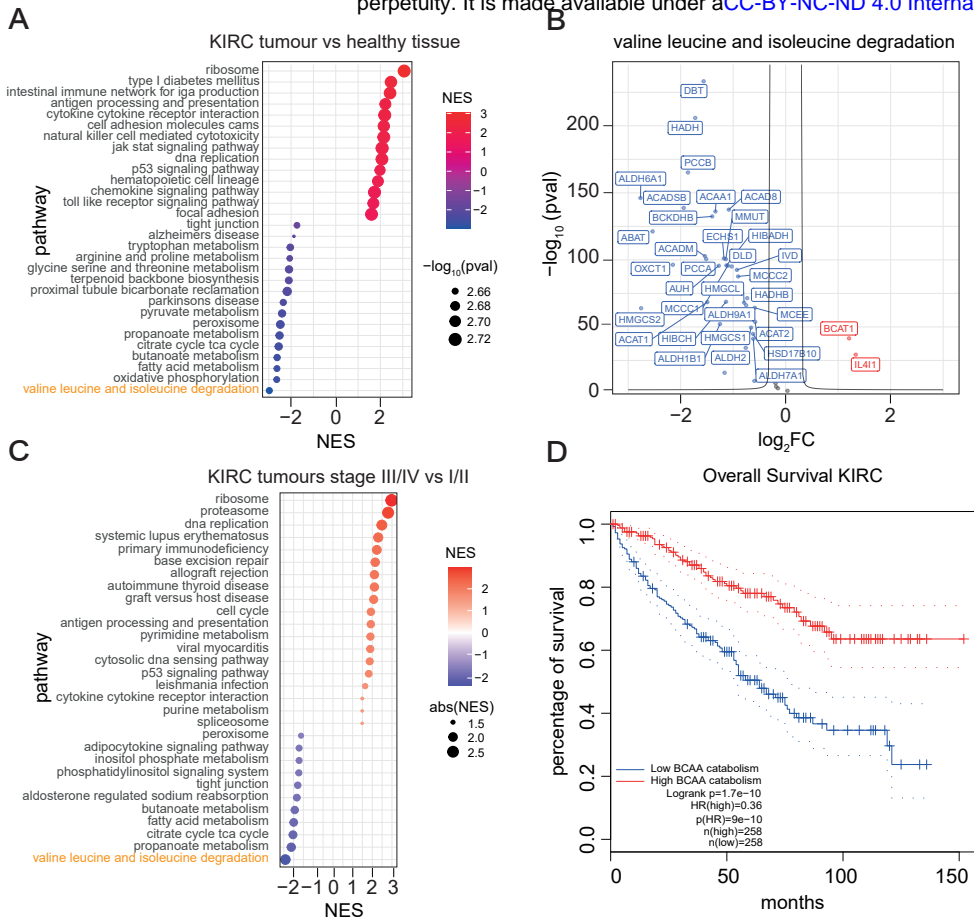
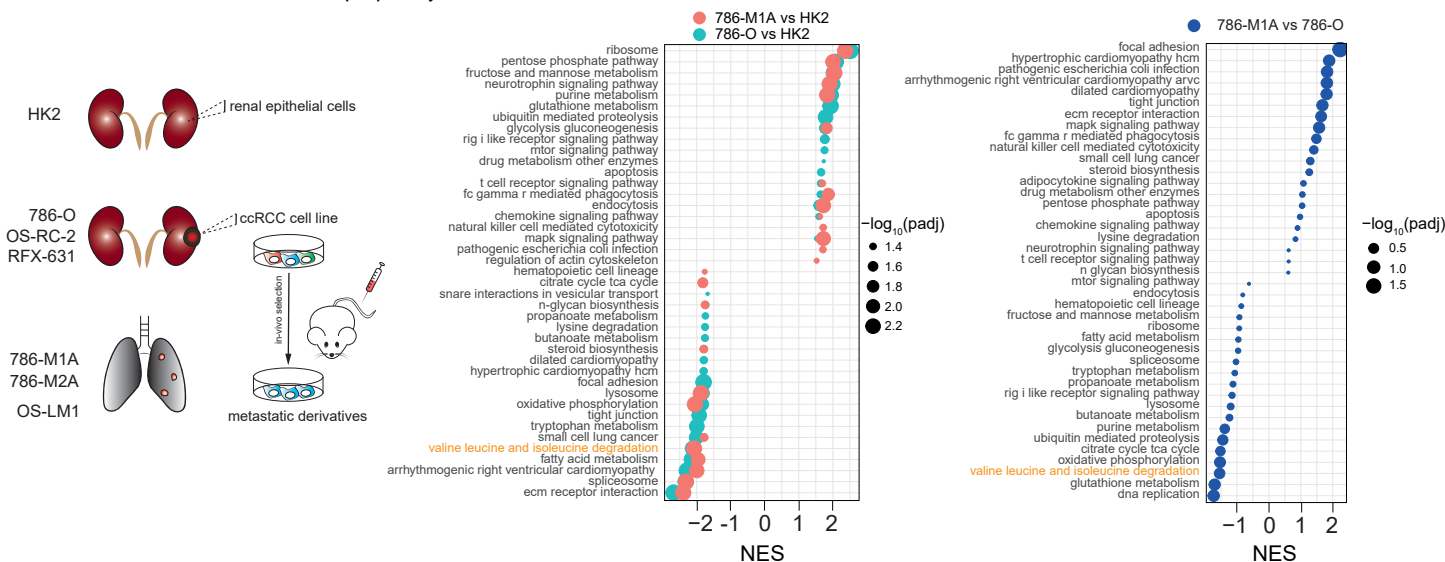
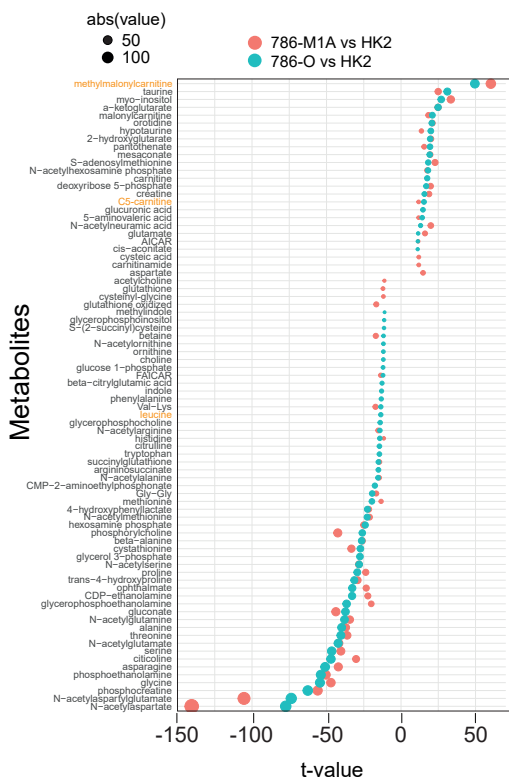


Figure 1. Branched-chain amino acids catabolism is suppressed in KIRC.

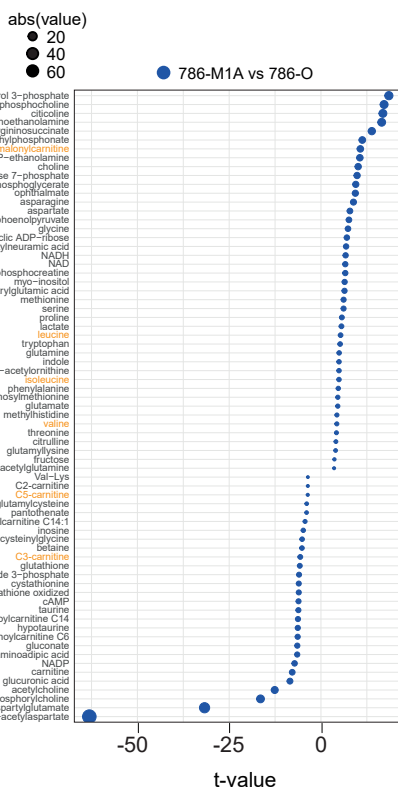
A



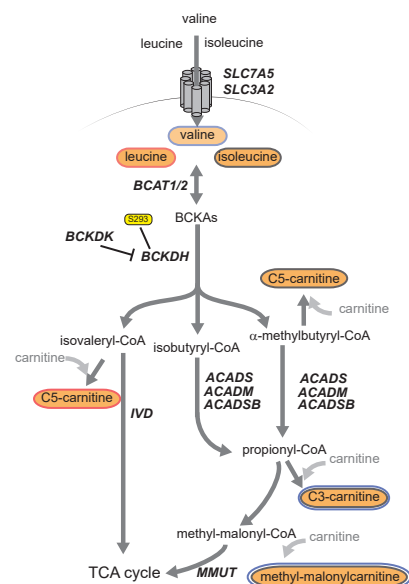
D



E



F



G

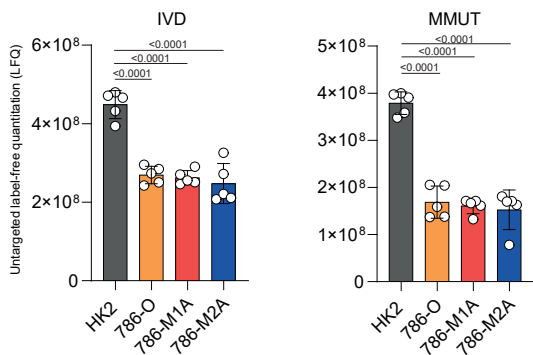


Figure 2. BCAA catabolism regulation in a cellular model system for renal cancer progression.

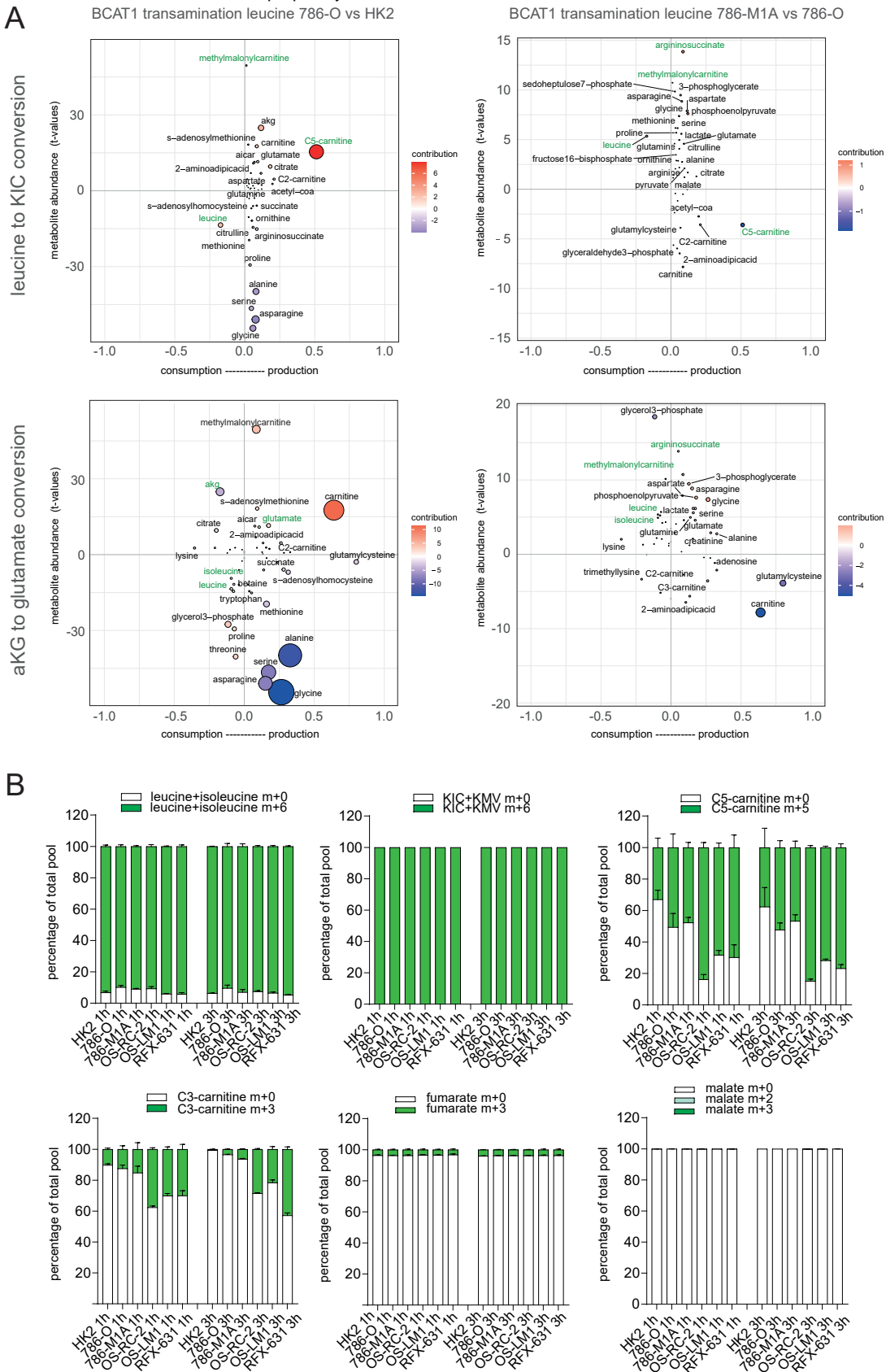
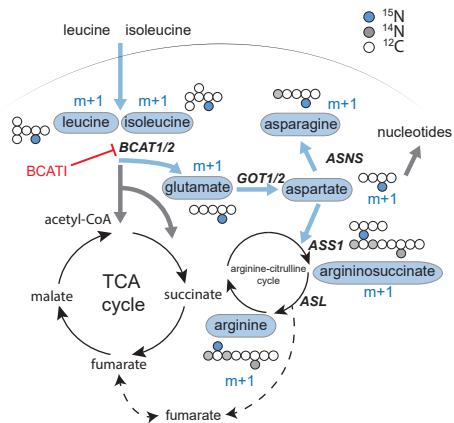
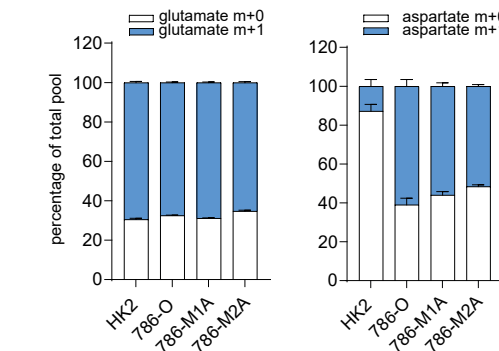


Figure 3. ocEAn, a tool to visualize metabolic changes in cancer cells.

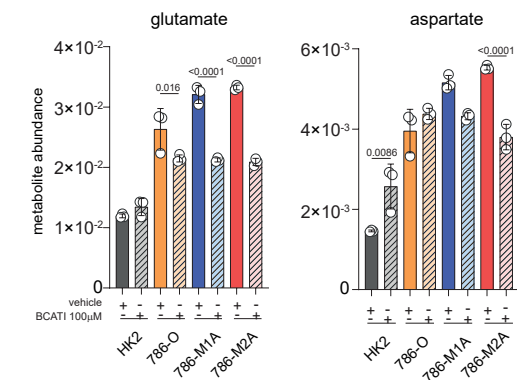
A



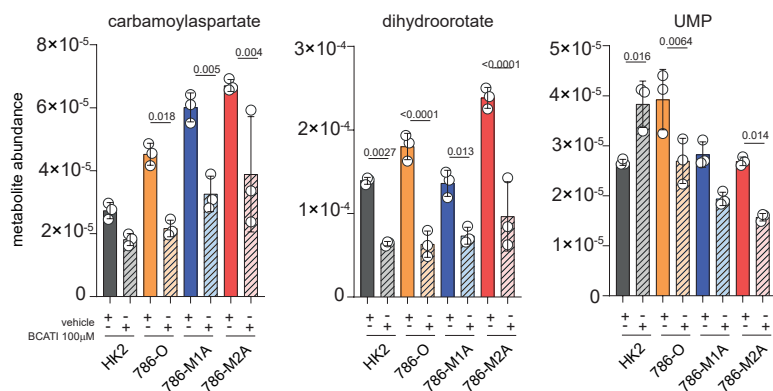
D



E



F



G

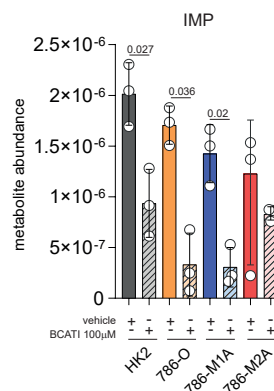
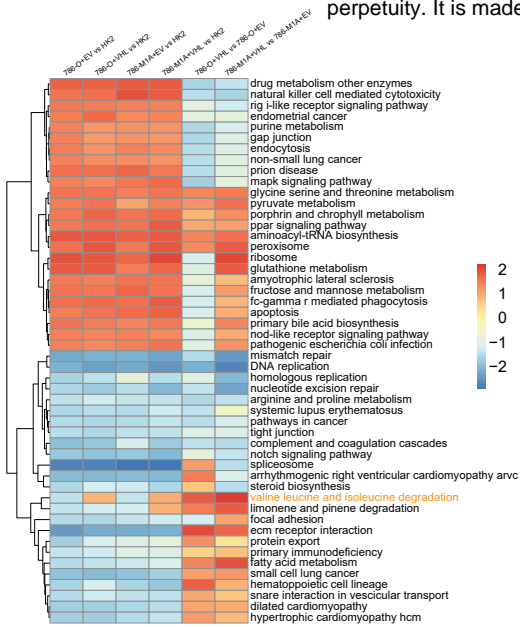
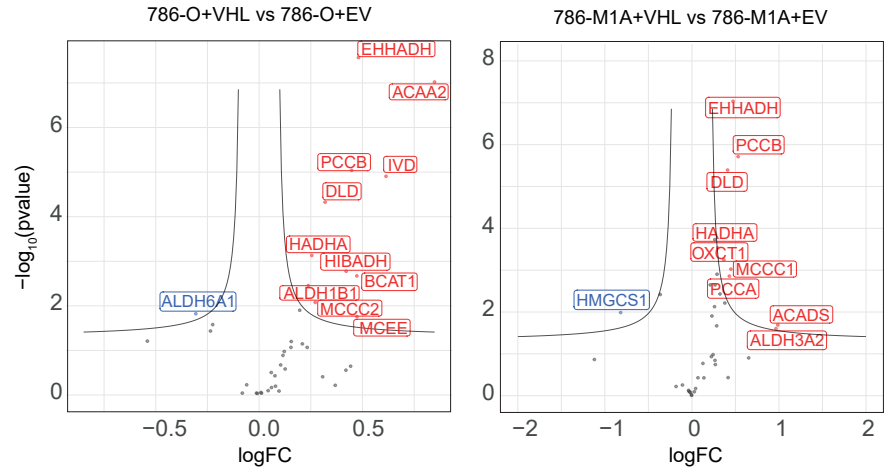


Figure 4. BCAT transamination supplies nitrogen for aspartate and nucleotide biosynthesis in ccRCC

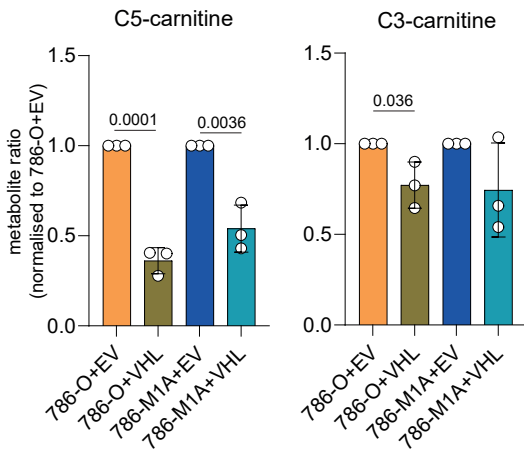
A



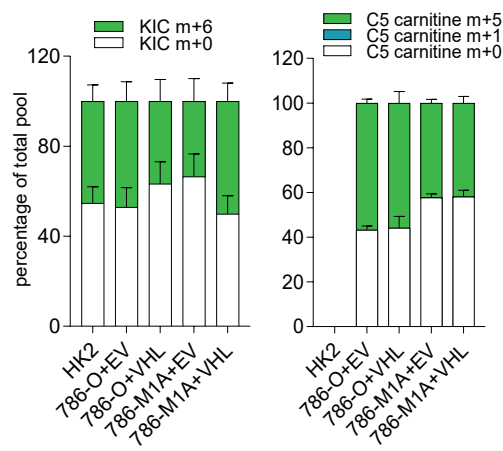
Valine, leucine and isoleucine degradation



C



D



E

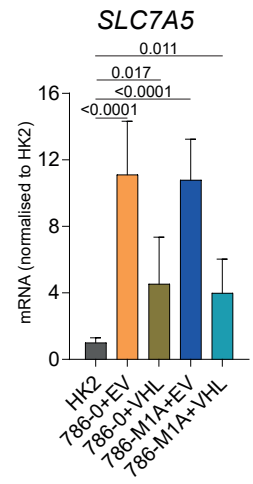


Figure 5. VHL reconstitution restored BCAA functioning in ccRCC cells.

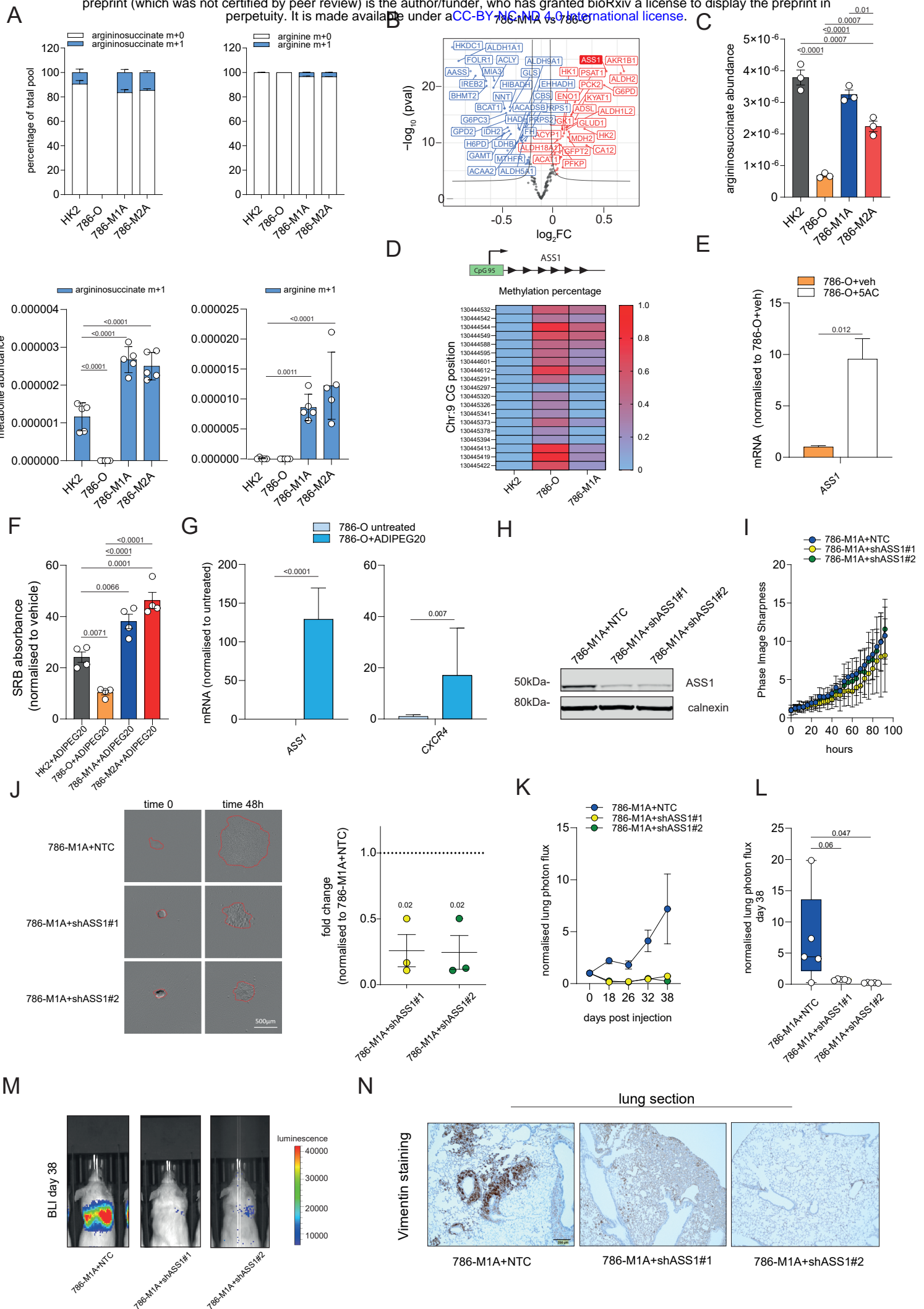


Fig.6 ASS1 re-expression in metastatic ccRCC confers resistance to arginine depletion and supports metastatic invasion *in vitro* and *in vivo*.

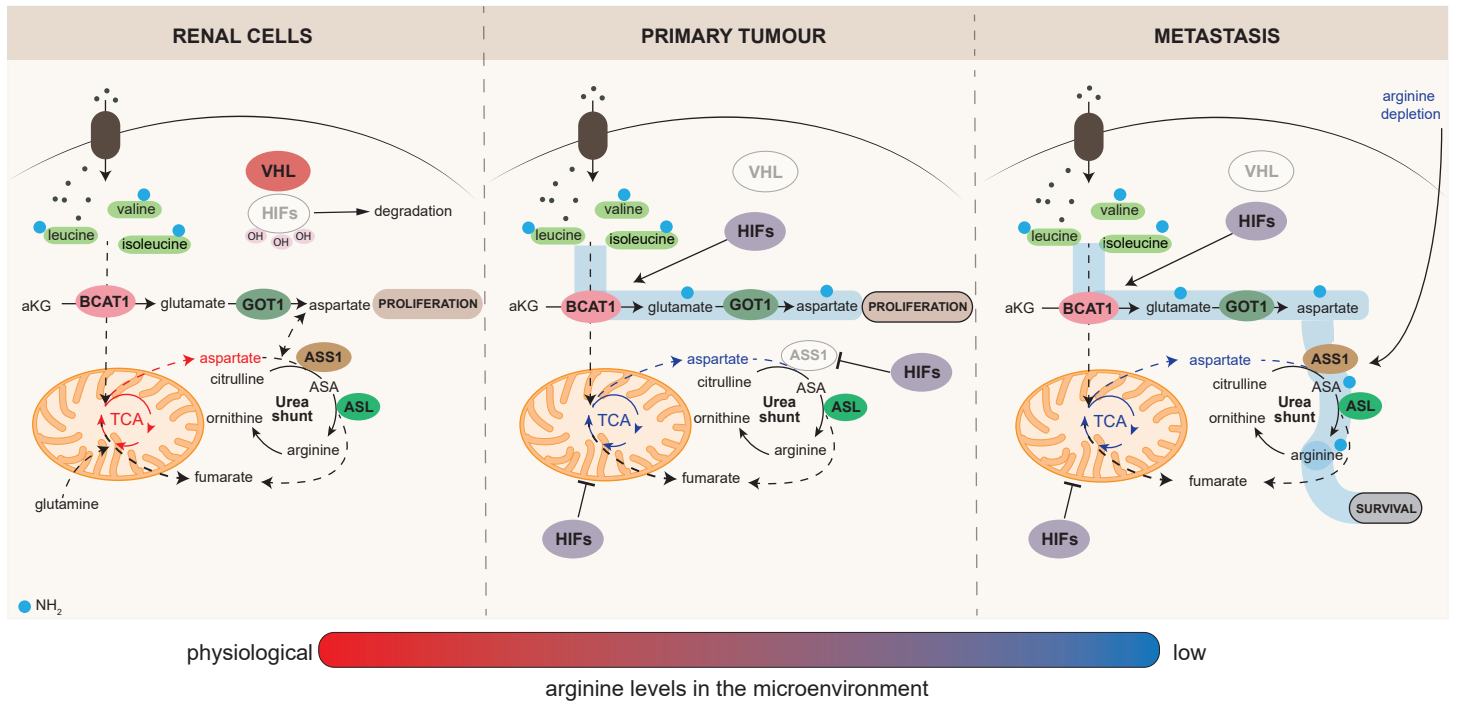
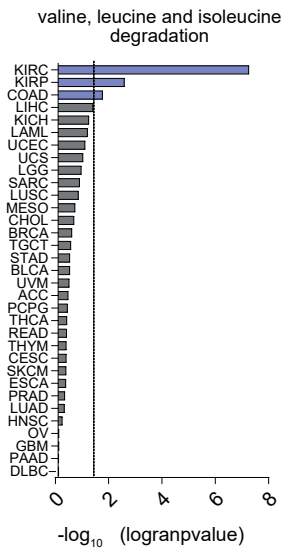
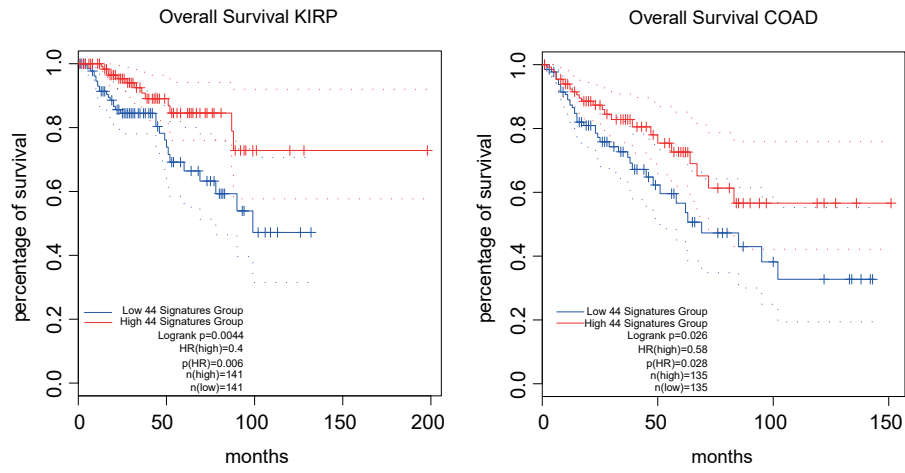


Figure 7. Reprogramming of the BCAA amino acid catabolism is intertwined with the urea cycle enzymes during ccRCC progression.

A

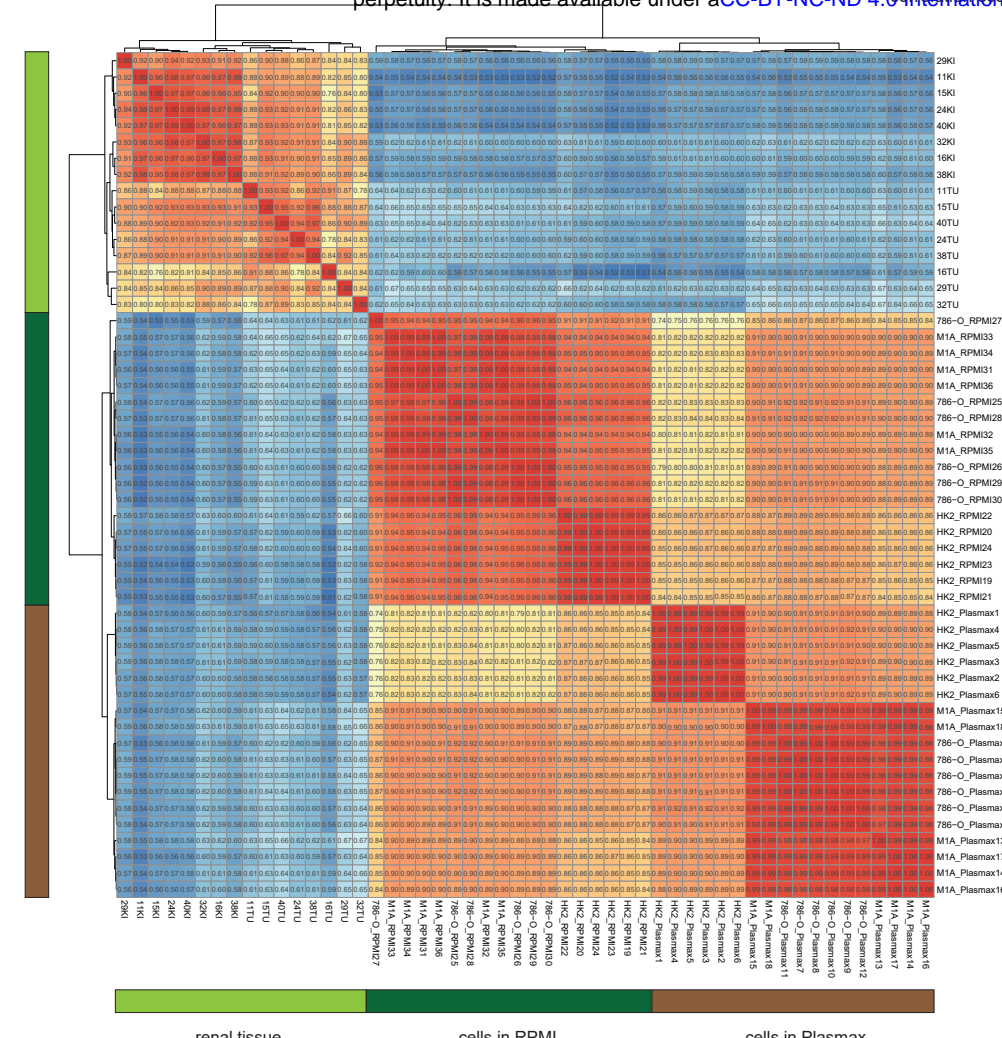


B

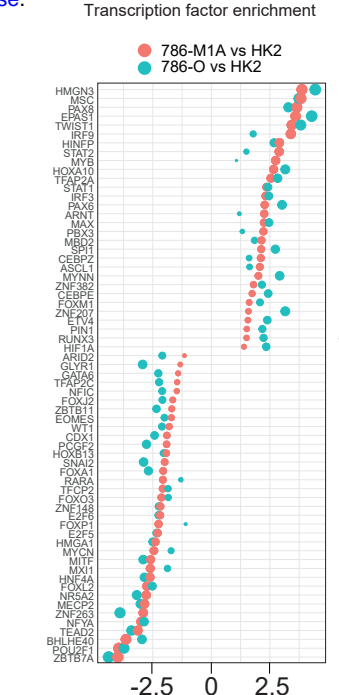


Supplementary Figure 1-related to Figure 1. Expression of the BCAA degradation pathway and TCGA patients' survival.

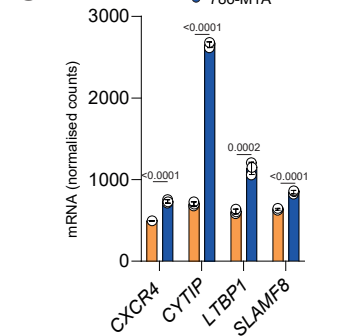
A



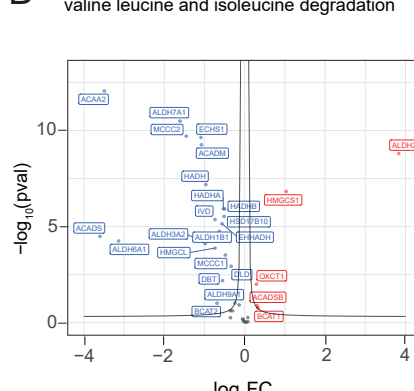
B



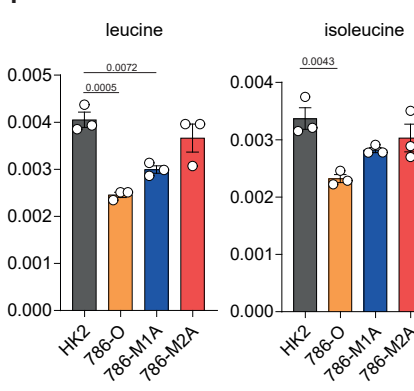
C



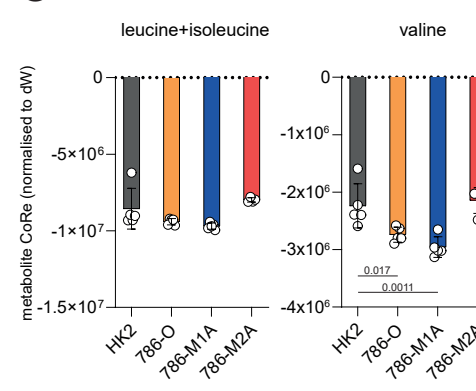
D



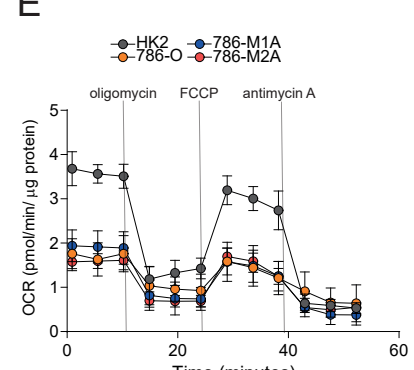
F



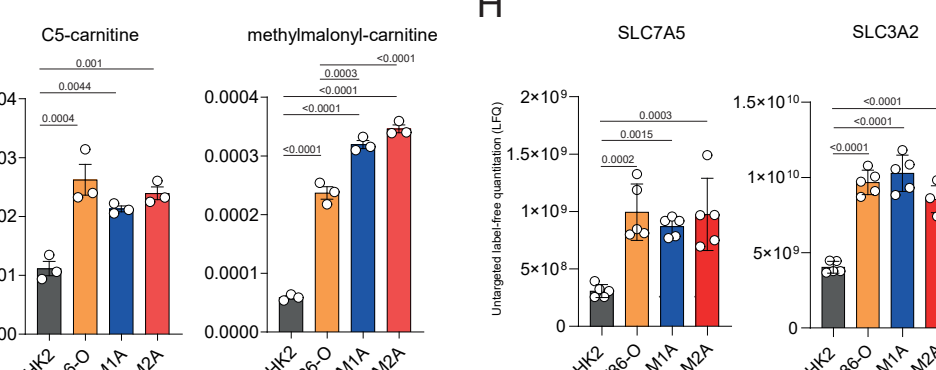
G



E

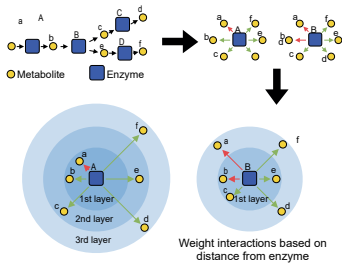


H

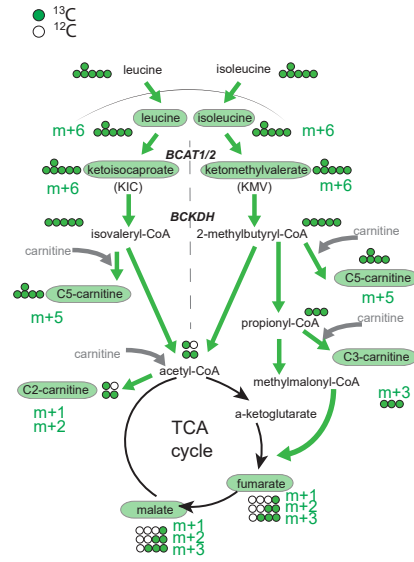


Supplementary Figure 2-related to Figure 2. ccRCC cells cultured in Plasmag resemble the metabolic and transcriptional profile of renal tumors

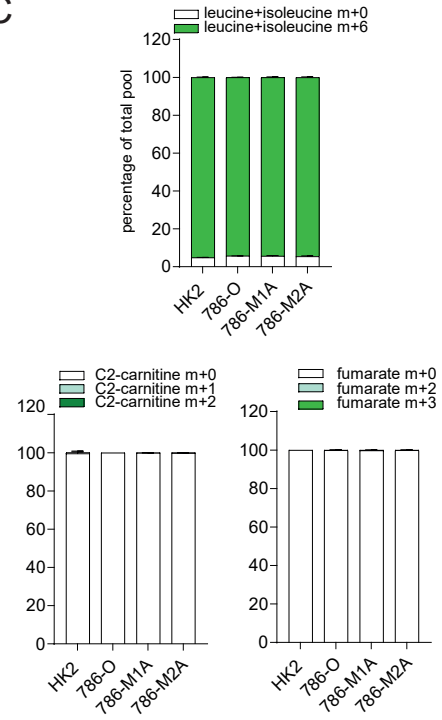
A



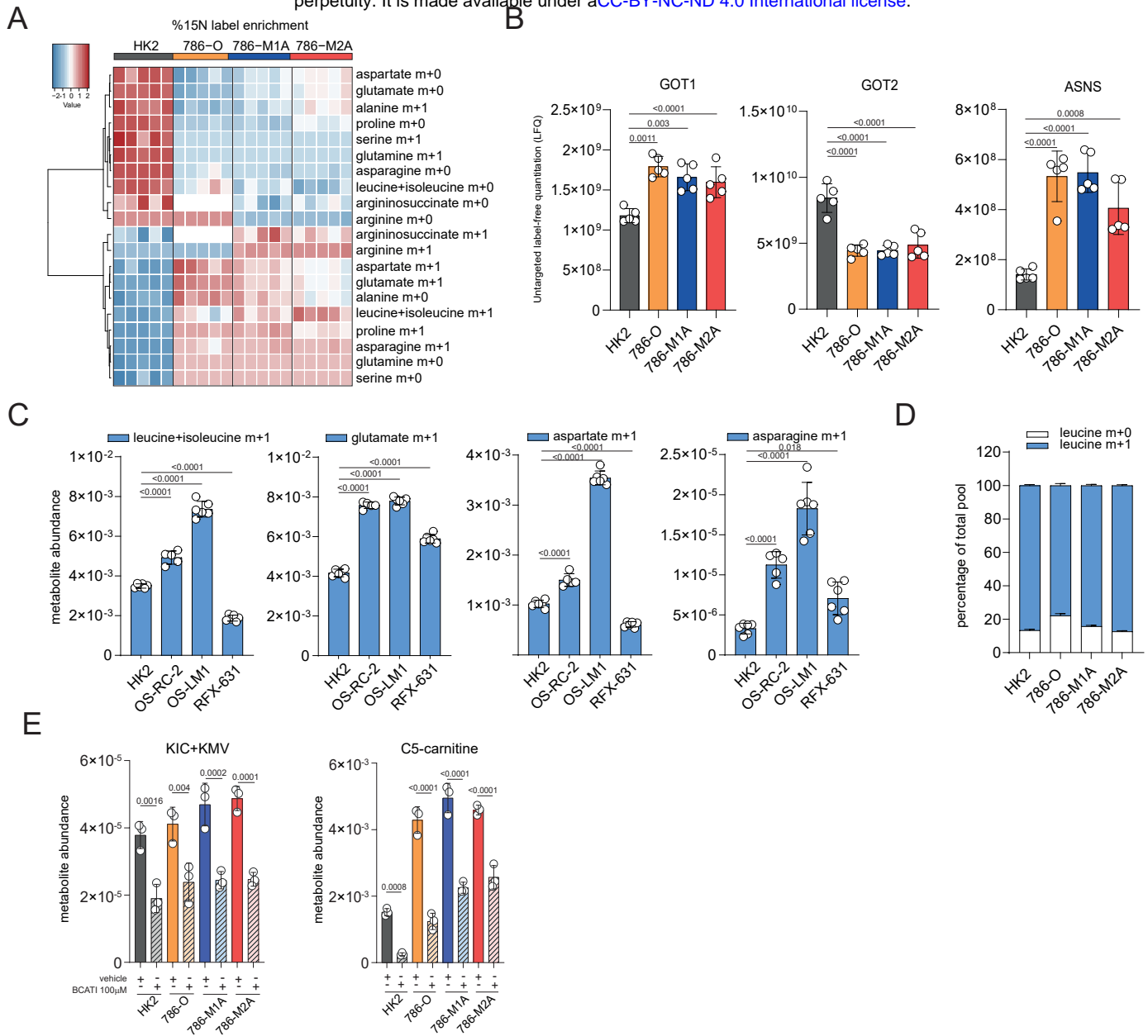
B



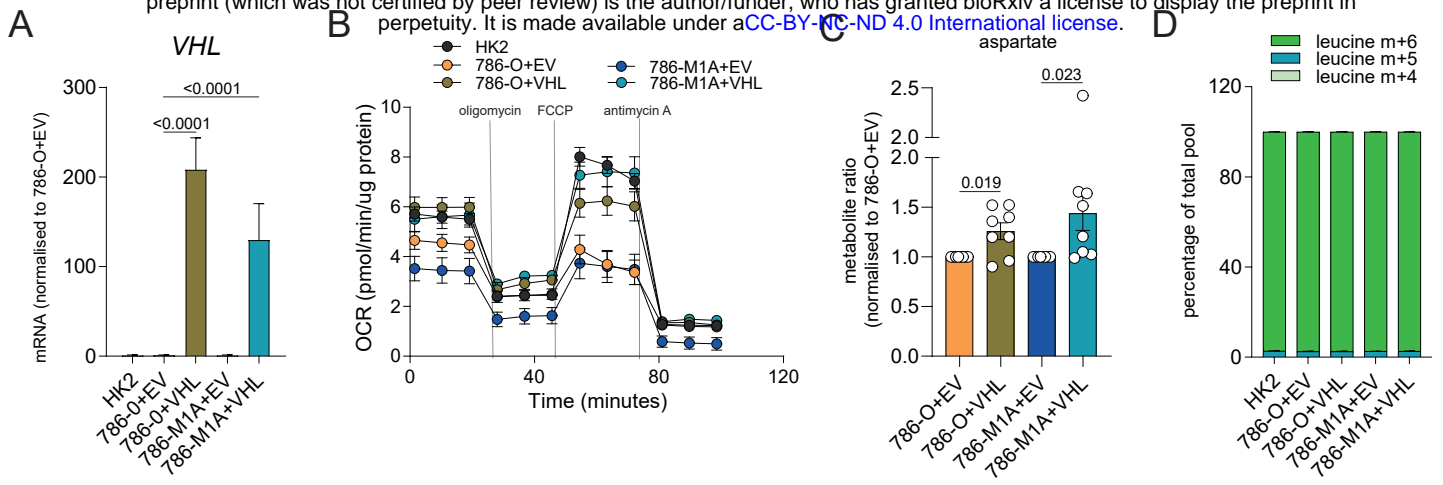
C



Supplementary Figure 3-related to Figure 3. BCAA catabolism does not provide carbons for the TCA cycle in ccRCC

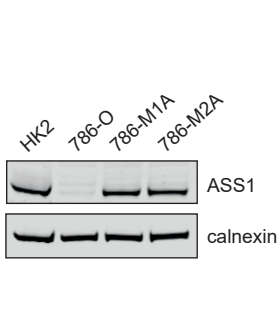
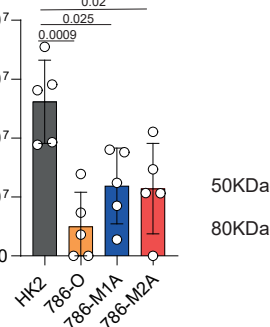
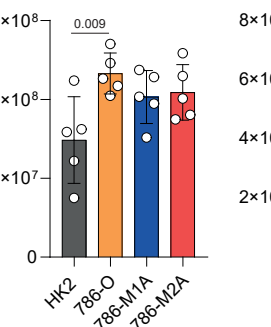
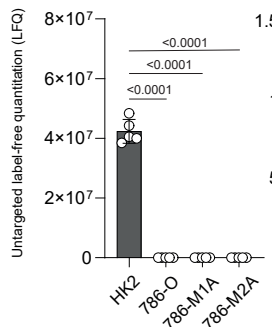
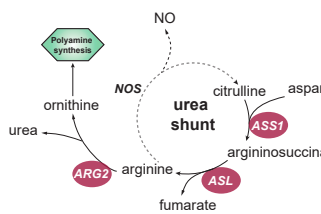


Supplementary Figure 4-related to Figure 4. BCAT transamination supplies nitrogen for aspartate synthesis in different ccRCC cell lines.

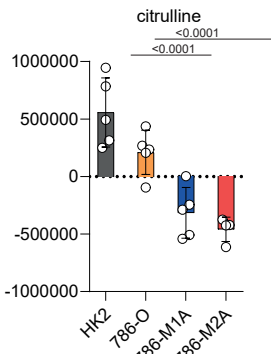
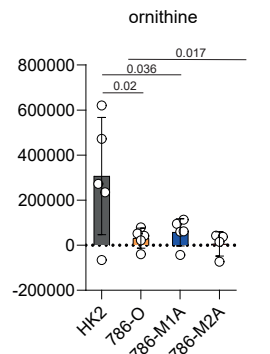
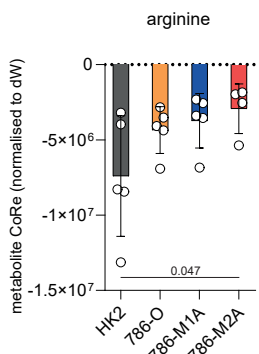


Supplementary Figure 5-related to Figure 5. VHL reconstitution restores mitochondrial function and aspartate level in ccRCC cells.

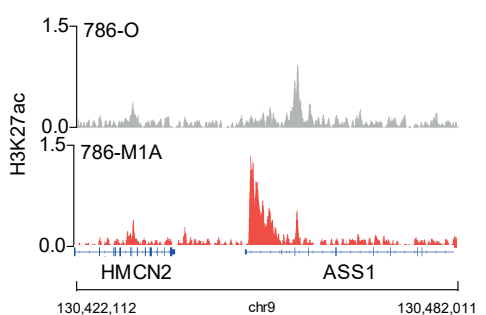
A



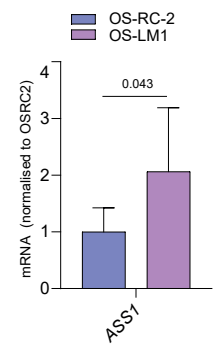
C



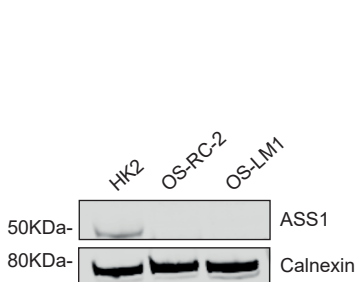
D



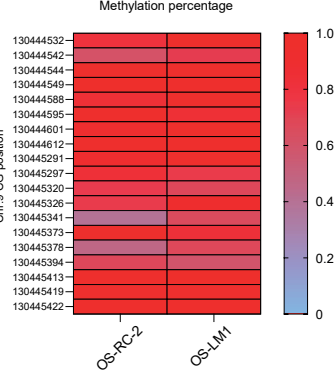
E



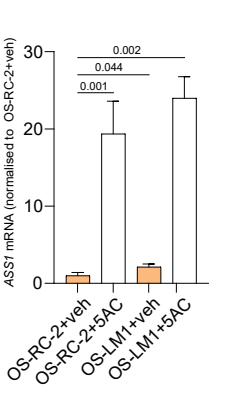
F



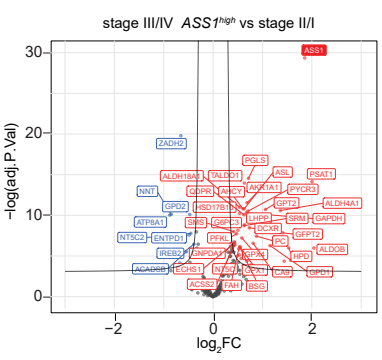
G



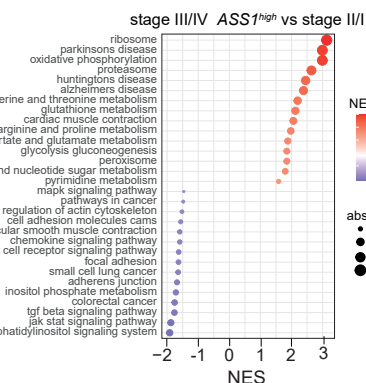
H



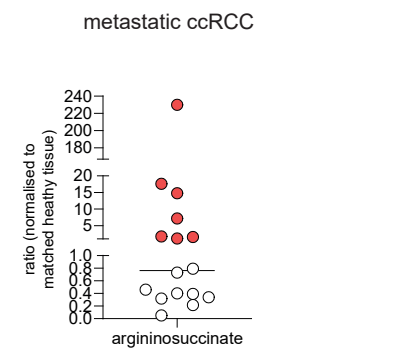
I



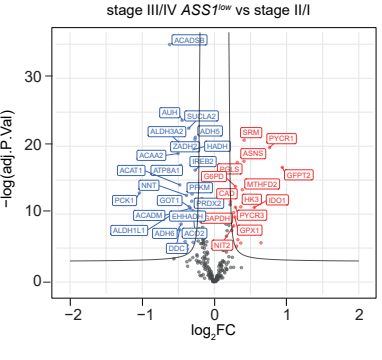
J



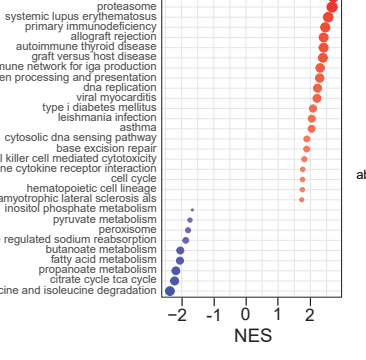
K



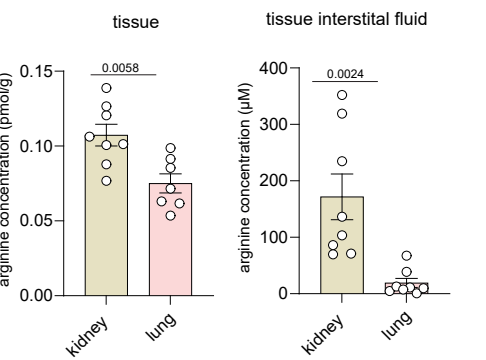
L



M



N



Supplementary Figure 6-related to Figure 6. ASS1 expression in metastatic OS-LM1 cells and advanced ccRCC tumors.